Engineering Structures 363 (2026) 123052

Contents lists available at ScienceDirect

Engineering Structures

journal homepage: www.elsevier.com/locate/engstruct

Experimental and analytical investigation of wind-induced response in a lighting tower

Andrea Orlando, Luisa Pagnini *, Maria Pia Repetto

DICCA – Polytechnic School, University of Genoa, Genoa, Italy

ARTICLE INFO

Keywords:
Long-term monitoring campaign
Steel monopole
Wind induced response
Wind field parameters
Drag coefficient
Aerodynamic damping
Uncertainty propagation

ABSTRACT

This paper presents the results of a long-term monitoring campaign on a 16.6 m steel lighting tower located at the Harbor of La Spezia, Italy. More than 5000 h of wind velocity, strain, and acceleration data were collected from which structural displacements were derived under varying wind conditions. The experimental evidence provides a robust benchmark for validating analytical gust-response models and for systematically addressing input uncertainties. The novelty of this research lies in: (i) the long-term full-scale monitoring data of a slender monopole under real environmental conditions; (ii) the combined use of strain- and acceleration-based techniques for displacement estimation; (iii) the quantification of parameter uncertainties by means of a three-level framework, ranging from code-based assumptions to site-specific measurements; and (iv) the explicit separation and quantification of model bias versus parameter bias in the dynamic response analytical estimation. Results highlight the sensitivity of the adopted analytical prediction to parameter accuracy and underscore the need for field data to support reliable assessment of wind-induced response of slender vertical structures.

1. Introduction

Slender structures and structural components are highly sensitive to wind excitation, which can induce vibrations in the longitudinal (along-wind), lateral (cross-wind), and torsional directions. Accurately predicting the wind-induced response of slender vertical structures remains a central challenge in wind engineering, as it directly affects both safety and serviceability.

Analytical frameworks provide a fundamental tool for estimating structural behavior under turbulent wind fields. Building on the pioneering contributions of Davenport [1–3], who developed the first method for calculating the along-wind displacement of vertical cantilever structures vibrating in their fundamental mode, subsequent formulations have progressively expanded the scope of the approach. These extensions include the evaluation of structural responses beyond displacements [4–8], the consideration of three-dimensional along-wind, cross-wind, and torsional effects [9–12], and the incorporation of aeroelastic phenomena [13]. Such calculation models are now also embedded in design codes and standards (e.g., [14,15]) for the most common structural typologies.

The accuracy of models is highly dependent on the precise definition of key input parameters, such as turbulence characteristics, aerodynamic coefficients, structural dynamics, and damping. These parameters are often subject to significant uncertainties, which can lead to overestimation or underestimation of the actual dynamic response. Such issues are evident in numerous documented cases of structural damage or failure in slender systems (e.g., [16–20]). While wind tunnel testing and numerical simulations have been widely adopted to mitigate these uncertainties (e.g., [21–24]), comprehensive full-scale validation studies remain scarce, especially for slender structures with ancillary components.

Full-scale monitoring campaigns have primarily focused on high-rise buildings (e.g., [25–27]., [28–32]) and long-span bridges (e.g., [33–36]). By contrast, only limited studies exist for slender monopole elements, such as lighting towers, under long-term monitoring regimes (e.g., [37–39]). A recent study on vortex-induced vibrations of a full-scale steel chimney [40] further highlights the importance of field measurements in capturing the dynamic response under realistic wind conditions.

Starting from these premises, a long-term, full-scale monitoring campaign was carried out on a 16.6 m slender steel lighting tower located at the Harbor of La Spezia. More than 5000 h of measurements were collected, including simultaneous data of wind velocity, strain, and acceleration. Adopting a novel data fusion approach, structural top

* Corresponding author.
E-mail address: luisa.pagnini@unige.it (L. Pagnini).

https://doi.org/10.1016/j.engstruct.2026.123052
Received 24 December 2025; Received in revised form 30 April 2026; Accepted 20 May 2026
Available online 27 May 2026

displacements were derived under varying wind loading conditions by combining acceleration and strain data. These experimental results serve both as a robust benchmark for validating analytical models and as a basis for systematically investigating input uncertainties. To assess the practical significance of these uncertainties, we focus on defining analysis levels that reflect different engineering approaches, quantifying the magnitude of errors an engineer may encounter in typical applications. To this end, the paper adopts a refined analytical model for predicting the dynamic response of poles and monotubular towers [41], which accounts for aerodynamic and aeroelastic effects caused by localized masses. Three levels of parameter accuracy are defined: a maximum level (Level 2), based on site-specific values derived from in-situ measurements and detailed analyses; an intermediate level (Level 1), using refined values from established methods in the literature; and a minimum level (Level 0), relying on simplified parameters from design codes and standards. This hierarchical framework enables an explicit quantification and discussion of uncertainties in the key parameters estimation. Moreover, comparing measured and predicted responses allows for the separation of model bias (inherent to the analytical formulation) from parameter bias (arising from input parameter uncertainties) in the dynamic response calculation.

The paper is structured as follows. Section 2 outlines the theoretical background of the dynamic response model for slender structures. Section 3 describes the monitoring system and the dynamic characterization of the lighting tower. Section 4 presents a novel methodology used to derive displacements from strain and acceleration measurements. Section 5 introduces the analytical procedure adopted to derive the dynamic response of the structure. Section 6 introduces the key input parameters at the three accuracy levels, discussing the associated uncertainties. Section 7 reports the comparison between analytical and experimental responses, emphasizing the distinction between model and parameter errors. Finally, Section 8 summarizes the main findings and discusses their implications for wind engineering practice.

2. Dynamic response of vertical slender structures under synoptic wind

The study of wind actions and their effects on structures is a cornerstone of civil engineering. Defining the appropriate analytical, experimental and numerical tools to evaluate wind-induced response, while ensuring safety, functionality, and sustainability is a key objective within the scope of wind engineering. Since the pioneering paper by Davenport [1], the "Davenport chain" has served as a foundational framework for understanding and calculating the dynamic response of wind-sensitive structures. The process begins with the evaluation of the wind velocity at the site.

In accordance with classical synoptic wind models, a Cartesian reference system x, y, z is defined, with its origin on the ground and the z-axis oriented vertically upward. The wind speed along z is described as:

$$u(z,t) = \boldsymbol{i}(\bar{\mathrm{u}}(z) + u'(z,t)) + \boldsymbol{j}v'(z,t) + \boldsymbol{k}w'(z,t) \tag{1}$$

where $\boldsymbol{i}$, $\boldsymbol{j}$, $\boldsymbol{z}$ are the unit vectors of x, y, z; $\bar{u}$ is the mean wind velocity parallel to the x-axis averaged over a time period T of 10 min or 1 h; u', v', w' are the longitudinal, lateral and vertical turbulence components, respectively parallel to the x, y, z axes.

The mean wind velocity profile is primarily governed by terrain roughness, topography, and atmospheric thermal stratification. Codes and most engineering applications assume that the surrounding terrain has homogeneous roughness, the atmosphere is neutral and describe the mean velocity profile using either a power law (e.g., [42]) or a logarithmic law (e.g., [15]).

Turbulence is modelled as a stationary Gaussian random field, usually represented in frequency domain by means of Power Spectral Density (PSD) and coherence [43] functions. Its accurate representation requires detailed knowledge of turbulence intensities and integral length scales.

The turbulence intensity of the γ' turbulence component, I_γ (γ=u, v, w), is defined as:

$$I_\gamma(z) = \frac{\sigma_\gamma}{\bar{\mathrm{u}}(z)} \tag{2}$$

where: σ_γ is the root mean square value of γ' over the period T.

The integral length scale of γ', L_γ (γ=u, v, w), is associated with the auto-correlation function of the turbulence component and provides a measure of the average size of the corresponding eddies; however, its modelling remains rather uncertain [44,45].

The cross-power spectral density function $S_{\gamma\gamma}$ of the fluctuating components is expressed by:

$$S_{\gamma\gamma}(z,z';n) = \sqrt{S_\gamma(z;n)S_\gamma(z';n)}Coh_\gamma(z,z';n) \tag{3}$$

where n is the frequency, S_γ is the power spectral density function and Coh_γ is the spatial coherence of γ'. Expressions for S_γ used for structural design purposes are given by, e.g., [46], Kaimal et al. [47], Simiu [48], Harris [49,50], Højstrup [51]. The spatial coherence for engineering purposes was originally given by Davenport [1] for the longitudinal turbulence in two points aligned along the vertical direction, and successively improved and extended (e.g., [52–57],[58]).

A slender vertical structure, modelled as a cantilever beam aligned with z, is subjected to aerodynamic actions along its structural axes which are resolved into along-wind (α=x) and cross-wind (α=y) components, F_α:

$$F_\alpha(z;t) = \overline{F}_\alpha(z) + F'_\alpha(z;t) \tag{4}$$

where $\overline{F}_\alpha$ is the mean aerodynamic force calculated over T, and F'_α is the fluctuating component. These forces give rise to along-wind and cross-wind horizontal displacements:

$$\alpha(z,t) = \overline{\alpha}(z) + \alpha'(z,t) \tag{5}$$

where $\overline{\alpha}$ is the mean displacement calculated over T; α' is the fluctuating component. In general, the dynamic response in Eq. (5) can be obtained using analytical, numerical and experimental tools. In the present paper, an advanced experimental procedure (Section 4) is proposed, based on a long-term, full scale monitoring of a slender pole (Section 3). In parallel, a refined analytical approach (Section 5) is adopted, capable of accounting for the effect of localized masses.

3. Full scale monitoring of a slender lighting pole

The analysed structure is a lighting tower consisting of a 16.6-meter-high steel pole (Fig. 1a) composed of two 16-sided polygonal sections connected by a telescoping joint (Fig. 1b). Each section is 5 mm thick and is formed by lamination and calendering of sheet metal, with the edges joined by a longitudinal weld having a throat depth of approximately 1 cm. The base and top diameters of the tower measure, respectively, 528 mm and 254 mm. The slenderness ratio is 45, calculated in accordance with guideline CNR [14]. The tower is equipped with a ladder running the full height of the pole, positioned on the side opposite the welded seam. At approximately 10 m height, a resting platform measuring 0.65 m × 1.0 m is installed. At the top of the pole, a squared platform (1.2 m × 1.2 m, and 1.1 m in height of the railing) houses the lighting equipment and a security camera. The lower portion of the pole is embedded in a 2.5 m high concrete cube, creating a clamped end.

The pole is located on a dam of the Harbor of La Spezia in Northern Italy in a quite complex non-homogeneous terrain (Fig. 2).

A monitoring system simultaneously measures wind speed and structural response. Specifically, a 3-axis ultrasonic anemometer is

Fig. 1. Global view of the tower (a); the polygonal shafts composing the tower (b).

installed on a 3-meter-high steel pole mounted on the top platform, at a height of z_{an}= 21.7 m above ground level. It provides high-resolution wind velocity data by recording the three components of wind speed at a sampling frequency of 10 Hz. Eight mono-axial strain gauges configured in a half-bridge design are installed at two different heights on the tower: 0.5 m and 1.5 m from the base. These form two monitored cross sections, each equipped with two pairs of sensors placed opposite each other along two orthogonal directions. Strain gauges measure the nominal vertical strain, enabling quantification of the structure's flexural deformation. The sampling rate is set at 100 Hz. Two biaxial MEMS accelerometers record the horizontal acceleration within an operating range of ± 2 g. They are positioned at the top of the pole, at 16.6 and at 11 m from the base, corresponding to the anti-nodes of the first and second bending mode, respectively. Data from the accelerometers are sampled at 200 Hz.

Fig. 3a shows a schematic of the tower and the sensor positions. Fig. 3b shows a cross section of the ensemble structural section and ladder indicating the structural axes η (the symmetry axis), and ζ (perpendicular to η), as well as the wind speed direction β with respect to the north. In particular, wind aligned with the η axis, with the ladder on the downwind side, corresponds to $\beta = 45°$; wind aligned with the ζ axis corresponds to $\beta = 135°$. Fig. 3c reports the first two mode shapes in plane η-z and ζ-z obtained from the free-vibration analysis of a finite element model representing the investigated structure, including the ladder and ancillary components [59].

A total of 5220 h of time-series data were collected over a three-year period, from 2019 to 2022, documenting 249 intense synoptic wind events with peak speeds exceeding 15 m/s. Additionally, 23 thunderstorm downbursts and gust front events were identified [60]; however, these are not the focus of the present analysis and are therefore not considered in this research. A comparison between downburst measurements and analytical wind load calculation methods is proposed by Mengistu and Repetto [61]. Fig. 4 provides a summary of the synoptic wind data, displaying the frequency distribution of wind direction (a), and of the mean and peak wind speed (b) based on 10-min time intervals.

4. Full-scale measurement-based estimation of structural displacement

Data fusion methods for displacement estimation require the combination of acceleration and strain data [62]. Strain gauges provide the mean displacement, while the fluctuating component can be derived from both accelerometers and strain gauges. Displacement can be obtained from acceleration by integrating the acceleration signal over time. Although this operation seems straightforward, the results are susceptible to noise and bias in the data. Such errors can accumulate during integration, potentially causing significant drift which affects the accuracy of the estimates, particularly in the quasi-static range [63]. Appropriate filters can mitigate these issues [64] when calibrated with distributed strain measurements (e.g., [65]). Zhu et al. [66] combine the strain-derived displacement with measured acceleration via a multi-rate Kalman filtering approach, while Zhou et al. [67] apply a FIR filter. Ma et al. [68] use an artificial neural network model automatically trained for strain–displacement transformation.

In the present case, strain measurements are available at only two levels along the structure. A simplified procedure, based on the Bernoulli–Euler beam equation, is therefore applied to obtain the displacement at any level of the pole from a single-level strain gauge record. Referring to Eq.(5), the mean displacement in the along-wind (α=x) and cross-wind direction (α=y) is expressed by:

$$\overline{\alpha}(z) = \kappa_{\alpha}(z) \quad f_{\alpha} \tag{6}$$

where f_α is a quantity related to the mean load; κ_α is dimensionless stiffness function modulating the displacement along z induced by the mean wind load.

Applying the principal transformation law and neglecting the contribution of higher vibration modes, the fluctuating component α' (α= x, y) can be expressed by:

$$\alpha'(z,t) = \psi_{1\alpha}(z)\, p(t) \tag{7}$$

where $\psi_{1\alpha}$ is the fundamental mode shape in the z-α plane, p is the principal coordinate.

Similarly to Eq.(1), the flexural strain along α is expressed as the sum

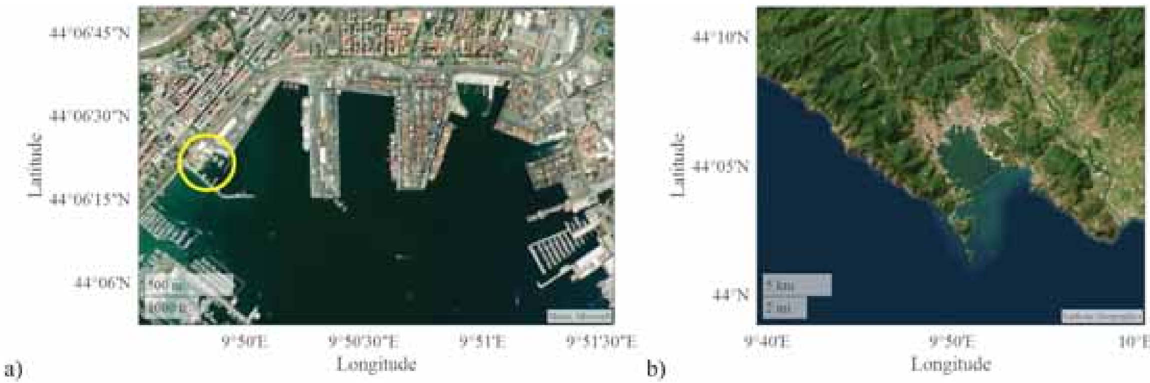

Fig. 2. Location of the pole: a) position of the structure inside the port area; b) orography of the surrounding region.

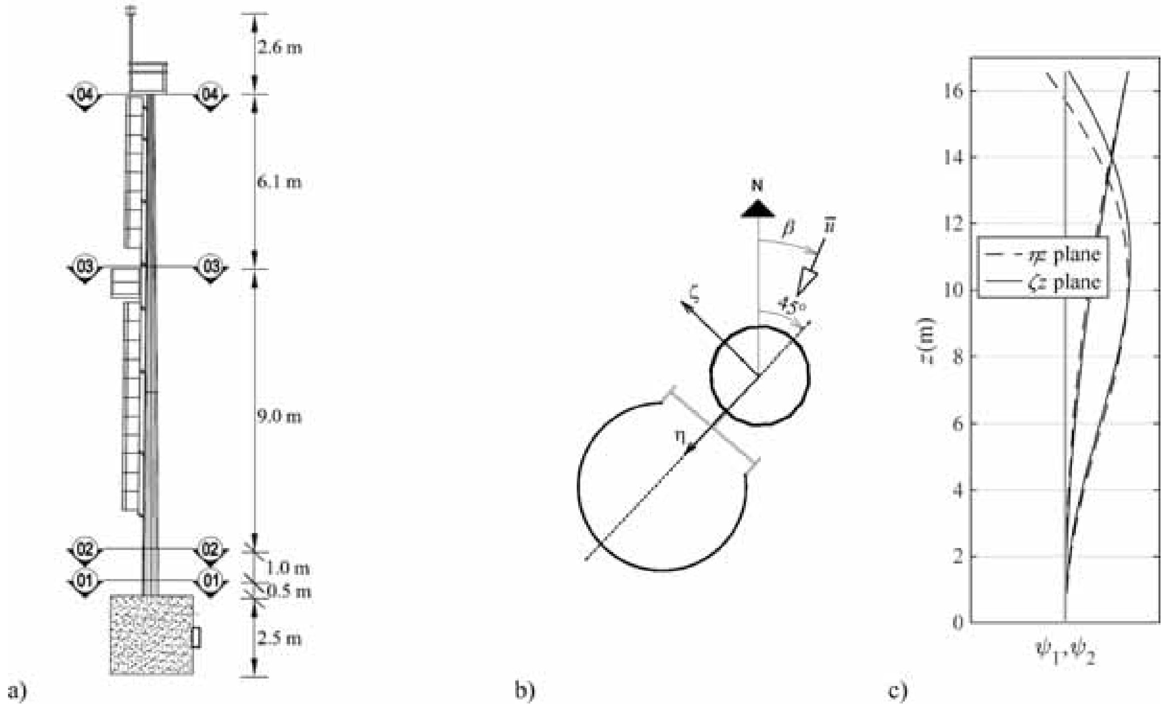

Fig. 3. Schematic of the structure: (a) elevation view with sensor positions; (b) cross section with ladder; (c) mode shapes.

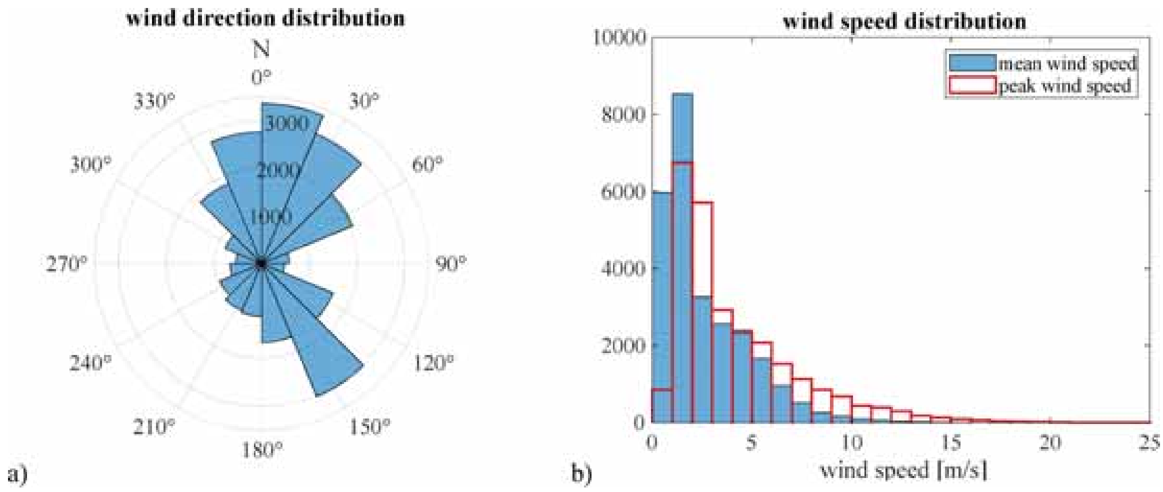

Fig. 4. Distribution of wind direction (a) and wind speed (b) in the dataset.

of a mean component, $\overline{\varepsilon}_\alpha$, associated to the mean load and fluctuating part, ε_α':

$$\varepsilon_\alpha(z,t) = \overline{\varepsilon}_\alpha(z) + \varepsilon_\alpha'(z,t) \tag{8}$$

Assuming pure biaxial bending in linear elastic field and using the Bernoulli–Euler beam equation, ε_α is related to the displacement along α by the equation:

$$\varepsilon_\alpha(z,t) = \frac{d^2\alpha(z,t)}{dz^2} r(z) \tag{9}$$

where r is the distance from the centroid of the cross section to the outermost point. The mean and fluctuating displacement at level z is related to the strain readings at level z_ε through the relationship [60]:

$$\overline{\alpha}(z) = \frac{\kappa_\alpha(z)\overline{\varepsilon}_\alpha(z_\varepsilon)}{\left.\frac{d^2\kappa_\alpha(z)}{dz^2}\right|_{z_\varepsilon} r(z_\varepsilon)} \tag{10}$$

$$\alpha'(z,t) = \varpi \frac{\psi_{1\alpha}(z)\varepsilon_\alpha'(z_\varepsilon,t)}{\left.\frac{d^2\psi_{1\alpha}(z)}{dz^2}\right|_{z_\varepsilon} r(z_\varepsilon)} \tag{11}$$

In Eq. (11), ϖ represents the fraction of the flexural strain that is effectively associated with the first modal contribution. The introduction of this coefficient is necessary because, although the assumption in Eq. (7) is generally considered valid for displacement calculations, other effects, such as the bending moment and, consequently, the strain, may include non-negligible contributions from higher modes [69–71].

In principle, strain measurements inherently contain the information required to estimate structural displacements, whereas accelerometer-based measurements tend to be less accurate at low frequencies. However, from a practical point of view, accelerometric measurements are generally more robust, and the derivation of displacements is more direct. For this reason, the present investigation derives the mean component of the structural displacement from strain measurements using Eq. (10), while the fluctuating components are determined by combining strain and acceleration data. Strain gauge data are used to characterize the low-frequency components, whereas accelerometer data are used for the higher frequency components. The procedure adopted is summarized as follows: displacement from accelerometers is obtained by double integrating the acceleration signal, whereas displacement from strain gauges is obtained using Eq. (11). A comparison between the Fast Fourier Transform (FFT) of the acceleration signal, $\tilde{\alpha}_{acc}$, and the strain record, $\tilde{\alpha}_{str}$, enables the identification of a frequency value, n_{comb}, that satisfies two conditions: (i) the resonant peak occurs at a frequency greater than n_{comb}; (ii) the discrepancy between the two FFTs at n_{comb} is below a predefined small threshold o. A new function $\tilde{\alpha}_{comb}$ is then derived to represent the FFT of the structural displacement, which combines both strain gauge and accelerometer data:

$$\tilde{\alpha}_{comb}(n) = \begin{cases} \tilde{\alpha}_{str}(n) & n \leq n_{comb} \\ \tilde{\alpha}_{acc}(n) & n > n_{comb} \end{cases} \tag{12}$$

The displacement time history is finally recovered by applying the inverse FFT to the combined spectrum $\tilde{\alpha}_{comb}$.

The application of this procedure is illustrated by estimating the along-wind structural displacement at the top of the pole from the 10-minute acceleration and strain records. The finite element model provides the modal shapes and enables the determination of κ_α by applying the load $\overline{F}_\alpha$.

In order to estimate the value of ϖ in Eq. (11), the role of first mode in ε'_α is estimated by expressing the displacement response through the modal transformation law. The spectral density of each principal coordinate is obtained as the product of the generalized force spectrum and the mechanical admittance [72]; the corresponding variance is computed through spectral integration over the low-frequency range of interest. The overall response related to each mode is finally reconstructed using the modal transformation law. While displacement contributions are governed by the eigenvectors, the bending moment, and therefore the strain, is weighted by the second spatial derivative of the mode shapes, thereby capturing the effect of local curvature. For the case considered, the contributions of the first and second modes to the base moment variance are about 80% and 20%, respectively; it corresponds to $\varpi = 0.9$

The relatively large role of the second mode is attributed to the characteristics of its modal shape, which exhibits a node near the tip and a pronounced curvature at the base, leading to a significantly enhanced influence on the base bending moment despite its small influence on the global displacement response.

Fig. 5a shows the FFT of the displacement at top obtained from acceleration ($\tilde{\alpha}_{acc}$, blue line) and from strain gauges ($\tilde{\alpha}_{str}$, red line); $o = 10^{-3}$ m·s, $n_{comb} = 0.7$ Hz.

It is observed that $\tilde{\alpha}_{acc}$ is much higher than $\tilde{\alpha}_{str}$ below the first resonant frequency, likely due to spurious components in the accelerometer measurements within the quasi-static range of the response. Near the first resonant frequency, the two functions almost overlap, supporting the validity of the modal-synthesis hypothesis. Above this frequency, they remain reasonably well aligned. In this range, accelerometers offer a more direct and accurate estimate of displacements. Fig. 5b presents the combined function $\tilde{\alpha}_{comb}$, which overcomes the low-frequency limitations observed in the accelerometer-based estimate.

It is noted that n_{comb} primarily depends on the characteristics of the accelerometers, particularly their valid frequency range, and on the fundamental frequency of the structure. Therefore, it should not be considered record-specific, but rather determined by the instrumentation and structural properties. Slight variations in the value of n_{comb} across different measurements are entirely negligible for the displacement estimation.

5. Analytical model-based estimation of structural displacement

The modelling of gust-excited structural response for routine engineering assessments is traditionally performed using the Gust Response Factor (GRF), defined as the ratio between the mean maximum dynamic response and the corresponding mean static response. Under the assumption of uncoupled motion components, α=x, y, the expected maximum wind-induced displacement in the along-wind and cross-wind directions over the time period T is given by:

$$\alpha_{\max}(z) = G_\alpha(z)\overline{\alpha}^x(z) \tag{13}$$

where$\overline{\alpha}^x$is the static displacement due to the application of $\overline{F}_x$ in direction α and G_α is the GRF. This method was proposed by Davenport [3] in its original formulation referred to the along-wind displacement of vertical cantilever structures, and successively developed, e.g., by Vickery [73], Simiu [74], Solari [75], Tamura et al., [76]. According to the so-called Equivalent Wind Spectrum Technique, the GRF was expressed in closed form [77] and extended to the cross-wind direction [10] according to the following relationships, with the subscript α=x, y indicating parameters referred to x and y direction:

$$G_x = 1 + 2g_x I_u(\overline{z})\sqrt{Q^2{}_x + R^2{}_x} \tag{14}$$

$$G_y = g_y I_v(\overline{z})\frac{|\overline{C}_D + \overline{C}'_L|}{\overline{C}_D}\sqrt{Q^2{}_y + R^2{}_y} \tag{15}$$

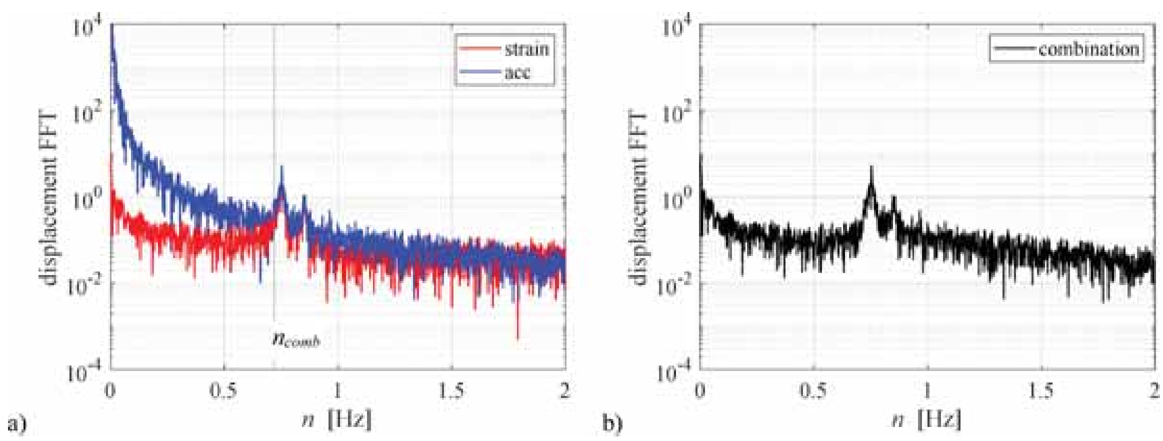

Fig. 5. Displacement FFT from strain gages and accelerometers (a); combined displacement FFT (b).

$$g_\alpha = \sqrt{2\ln[\Lambda_\alpha \upsilon_\alpha T]} + \frac{0.5772}{\sqrt{2\ln[\Lambda_\alpha \upsilon_\alpha T]}} \tag{16}$$

$$\upsilon_\alpha = n_{\alpha 1}\sqrt{\frac{R^2{}_\alpha}{Q^2{}_\alpha + R^2{}_\alpha}} \tag{17}$$

where Q_α and R_α are non-dimensional quantities associated respectively to the quasi-static and resonant parts of the response; g_α and υ_α are the peak factor and the expected frequency; I_u and I_v are the longitudinal and lateral turbulence intensity; $\bar{z}= 0.6\ h$, where h is the height of the structure; $\overline{C}_D = C_D(\bar{z})$, being C_D the drag force coefficient of the pole, $\overline{C'}_L = C'_L(\bar{z})$, being C'_L the prime angular derivative of the mean lift force coefficient; $\Lambda_x= 1$, $\Lambda_y= 2$.

The static displacement is expressed by:

$$\overline{\alpha}^x = \psi_{1\alpha}(z)\frac{\rho\overline{u}^2(\bar{z})\overline{b}h\psi_{1\alpha}(h)}{2m_{1\alpha}(2\pi n_{1\alpha})^2}\overline{C}_D\overline{K}_{\alpha x} \tag{18}$$

where ρ is the air density, $m_{1\alpha}$ is the modal mass, $\overline{b} = b(\bar{z})$, with b a reference dimension of the cross section, and $\overline{K}_{\alpha x}$is an appropriate non-dimensional coefficient. For α=x, $\overline{\alpha}^x = \bar{x}$.

This paper adopts the subsequent generalization to poles and monotubular towers that considers the presence of ν localized masses, simulating lighting fixtures and other ancillaries, and aeroelastic terms in the quasi-static and resonant parts of the response [41]:

$$\overline{K}_{\alpha x} = \Delta_0 + \sum_{k=1}^{\nu}\Delta_k \tag{19}$$

$$Q_\alpha = \frac{1}{\overline{K}_{\alpha x}}\left(K'_0 Q_{0\alpha} + \sum_{k=1}^{\nu}K'_{k\alpha}Q_{k\alpha}\right) \tag{20}$$

$$R_\alpha = \frac{1}{\sqrt{2\pi\xi_{1\alpha}}}\frac{1}{\overline{K}_{\alpha x}}\left(K'_0 D_{0\alpha} + \sum_{k=1}^{\nu}K'_{k\alpha}D_{k\alpha}\right) \tag{21}$$

where Δ_0 and Δ_k are dimensionless coefficients related to the shaft and to the kth localized mass; $Q_{0\alpha}$ and $D_{0\alpha}$ are quasi-static and resonant parameters associated to the aerodynamic actions on the pole; similarly, $Q_{k\alpha}$ and $D_{k\alpha}$ are quasi-static and resonant parameters associated to the aerodynamic actions on the kth localized mass; K'_0 and $K'_{k\alpha}$ are additional non-dimensional coefficients. $\xi_{1\alpha}$ the is first modal damping ratio, defined as the sum of the structural, $\xi_{1s\alpha}$, and the aerodynamic component, $\xi_{1A\alpha}$, which depends on wind speed, aerodynamic and structural properties [58]. In presence of localized masses, $\xi_{1A\alpha}$ can be calculated by:

$$\xi_{1Ax} = \frac{\rho\overline{u}(\bar{z})\overline{b}h\overline{C}_D\psi^2{}_{1x}(h)}{4\pi n_{1x}m_{1x}}\left(K''_{0x} + \sum_{k=1}^{N}K''_{kx}\right) \tag{22}$$

$$\xi_{1Ay} = \frac{\rho\overline{u}(\bar{z})\overline{b}h(\overline{C}_D + \overline{C}'_L)\psi^2_{1y}(h)}{8\pi n_{1y}m_{1y}}\left(K''_{0y} + \sum_{k=1}^{N}K''_{ky}\right) \tag{23}$$

withK''_{0x},K''_{0y},K''_{kx},K''_{ky} non-dimensional coefficients supplied in [41].

The adopted approach relies on a number of simplifying assumptions that deserve further consideration. In particular, the decoupling of motion components in the longitudinal and transverse directions may not be strictly valid when the wind direction is not aligned with the structure's principal axes of inertia. Under such circumstances, torsional components may also arise due to mass eccentricities, such as ancillary elements or appendages mounted along the pole. Moreover, the GRF method assumes that the wind-induced response is adequately represented by the contribution of the first vibration mode only. Although this assumption may introduce some inaccuracies when estimating other response quantities, such as accelerations, it is generally appropriate for the evaluation of structural displacements [11,78]. Finally, it is worth noting that the response model does not extend to cases of non-stationary non-Gaussian wind, which are addressed in other studies (e.g., [61]).

6. Parameter uncertainties

The application of Eqs. (13) – (23) requires knowledge of several parameters, including wind-related, aerodynamic, and dynamic structural parameters. These quantities can be derived from anemometer and structural response measurements; however, for engineering design, they are more commonly estimated using predictive models available in the literature or specified in design guidelines. Regardless of the estimation method, these parameters are affected by uncertainties arising from inherent variability or limited knowledge, which propagate through the structural response evaluation and ultimately influence the reliability of the results (e.g., [79–81]).

In this study, the input parameters are obtained from in-situ measurements, limited to stationary synoptic events, and supplemented with predictive models and established guidelines. Among the wind-related parameters, attention is given to the mean wind velocity, turbulence intensity, and integral turbulence scale. The aerodynamic parameter considered is the drag coefficient, while the structural parameters include the modal shape, natural frequency, and damping ratio.

With the dual purpose of assessing the reliability of the calculation model for the gust excited response of the lighting pole and of analyzing the impact of parameter uncertainties, the input parameters are determined according to three different levels of accuracy. At the highest accuracy level, designated as Level 2, they are evaluated from in-situ measurements and, when necessary, supplemented with refined methods available in the literature. At accuracy Level 1, parameters are estimated exclusively using refined analytical or empirical methods from the literature. At the simplest accuracy level, Level 0, parameters are obtained from the simplified models prescribed in current regulations and standards. Investigations are carried out for stationary synoptic wind only, aligned with the η and ζ principal axes.

Table 1 summarizes the procedure used to estimate the selected quantities according to the three adopted accuracy levels, as discussed in the following Sections.

6.1. *Wind field parameters*

The 10-min mean wind velocity can be directly estimated from the anemometric measurements at the height z_{an}. At Level 2, the mean wind profile is estimated for 18 directional sectors, each 20° wide, following to the procedure outlined in ESDU 84011 [82], and modelling terrain roughness up to a distance of 20 km from the pole location. Fig. 6a shows the roughness values in the area; the corresponding mean wind profiles normalized to the value at the anemometer are reported in Fig. 7 (colored circles).

At Level 1, an equivalent terrain roughness $z_{0\beta,e}$ is calculated for wind blowing from each sector β using ESDU 84011. The normalized

Table 1
Parameter estimation according to the three adopted accuracy levels.

accuracy level	wind profile	I_u , L_u	drag coefficient	damping
Level 2	ESDU 84011, (directional)	in-situ measurements	from wind tunnel measurements	from measurements, applying EFDD
Level 1	logarithmic law; z_0 from ESDU 84011 (directional)	from Solari and Piccardo [45]; z_0 from ESDU 84011 (directional)	ESDU 79026	from Solari and Pagnini [41]
Level 0	CNR-DT 207	CNR-DT 207	CNR-DT 207 circular cylinders	CNR-DT 207 unlined steel stacks

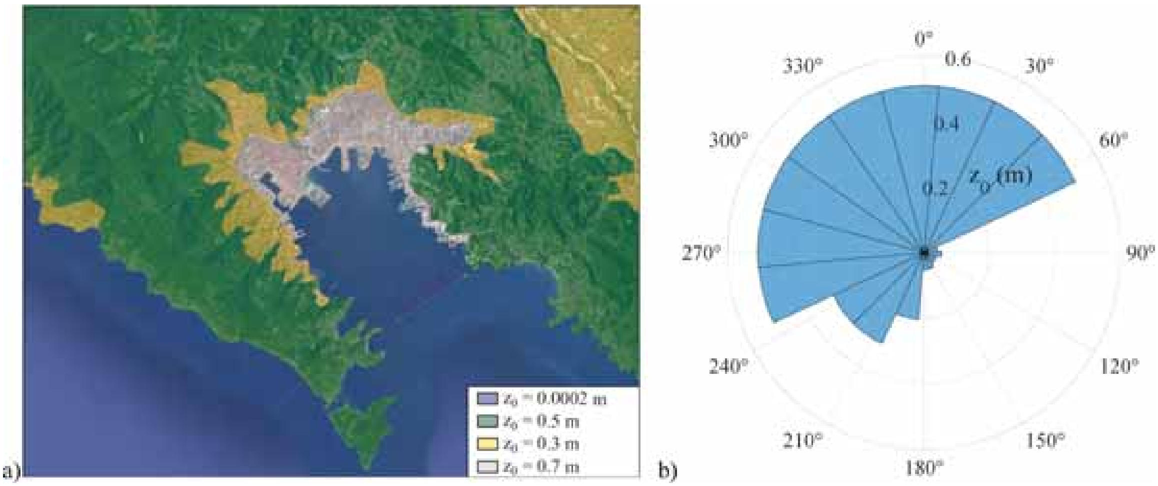

Fig. 6. Terrain roughness of the selected location according to ESDU 84011 (a) and equivalent roughness (b).

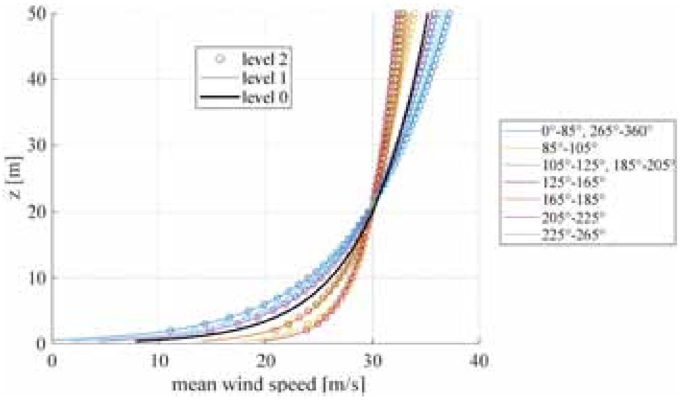

Fig. 7. Mean wind profile normalized at the anemometer height z_{an} at the three accuracy levels.

mean wind profile for the 18 directional sectors is then described by the logarithmic law:

$$\frac{u(z,\beta)}{u(z_{an},\beta)} = \frac{\ln\left(z/z_{0\beta,e}\right)}{\ln\left(z_{an}/z_{0\beta,e}\right)} \tag{24}$$

Fig. 6b shows the resulting equivalent roughness values, while the corresponding mean wind profiles are reported in Fig. 7 by the colored lines.

At Level 0, the mean wind profile is obtained by the logarithmic law applied in accordance with Italian Guidelines CNR-DT 207 [14], exposure category III, assuming an average terrain roughness of $z_0 = 0.1$ m, regardless of wind direction. In Fig. 7, the black thick line represents the corresponding mean wind profile.

The diagrams in Fig. 7 indicate that the estimates obtained at accuracy Levels 2 and 1 are in close agreement, particularly below the anemometer height, while also revealing a marked directional dependence. The Level 0 wind profile provides a direction-averaged reference trend.

Turbulence intensity is generated by thermal and shear effects, related, respectively, to the atmospheric stability and to the terrain roughness. The dependence on z_0 becomes significant at high wind speeds, where the atmosphere tends to be neutral. At Level 2, it is estimated from the anemometric records by applying Eq. (2) to the 10-min wind speed data. At Level 1, and under the assumption of neutral atmospheric conditions, it is estimated for the different sectors β using the following relationship:

$$I_\gamma\left(z,\beta\right) = \frac{k_\gamma}{\ln\left(z/z_{0\beta,e}\right)} \tag{25}$$

where γ=u,v, k_u= 1, k_v= 0.78 [45]. At Level 0, turbulence intensity is estimated using Eq. (25), assuming $z_0 = 0.1$ m.

The integral length scale of the turbulence components also depends on thermal and shear effects. At Level 2, it is determined from the anemometric measures, using both power spectra and correlation, as outlined by Flay and Stevenson [83]. At Level 1, under the assumption of neutral atmospheric conditions, it is obtained using the following relationships [45]:

$$L_u\left(z,\beta\right) = 300(z/300)^{d_\beta}; \qquad L_v = 0.25\ L_u \tag{26}$$

$$d_\beta = 0.46 + 0.074\ \ln\left(z_{0\beta,e}\right) \tag{27}$$

At Level 0, it is obtained using Eqs. (26), (27), irrespective of wind direction, with $z_0 = 0.1$ m.

Fig. 8 and Fig. 9 show the values of the longitudinal turbulence intensity and the integral length scale at the anemometer height obtained from the entire database at the three accuracy levels, as a function of the mean wind velocity (a) and mean wind direction (b).

Values directly derived from the measurements (Level 2, red circles) exhibit significant dispersion, particularly at low wind velocities, due to the thermal effects. As the mean wind velocity increases, atmospheric condition approaches neutrality and values align more closely with the estimates at Level 1 (reported for the different sectors by the solid blue

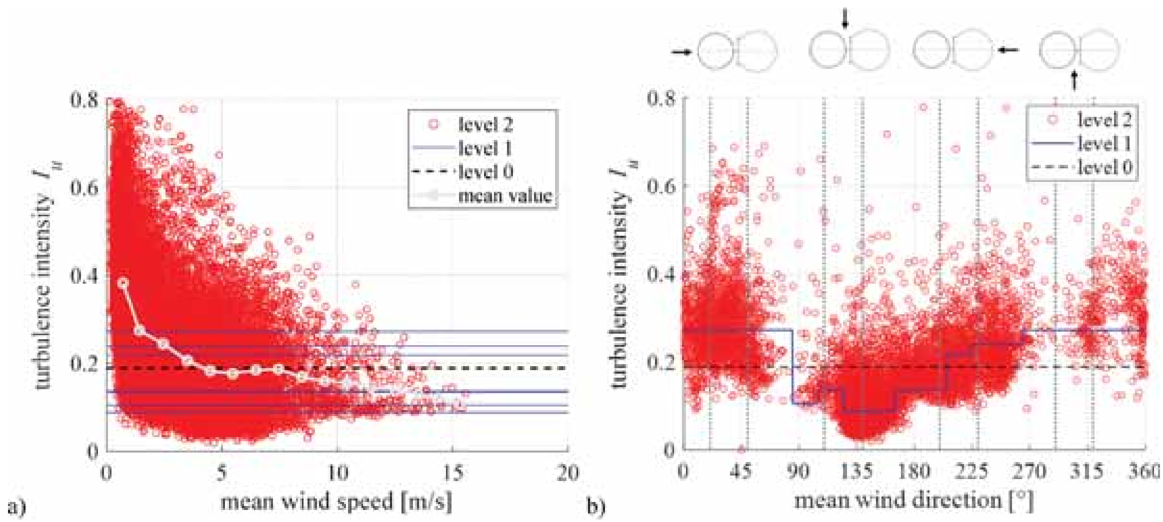

Fig. 8. Longitudinal turbulence intensity at the anemometer height, evaluated with the three accuracy levels: a) versus mean wind velocity, b) versus mean wind direction.

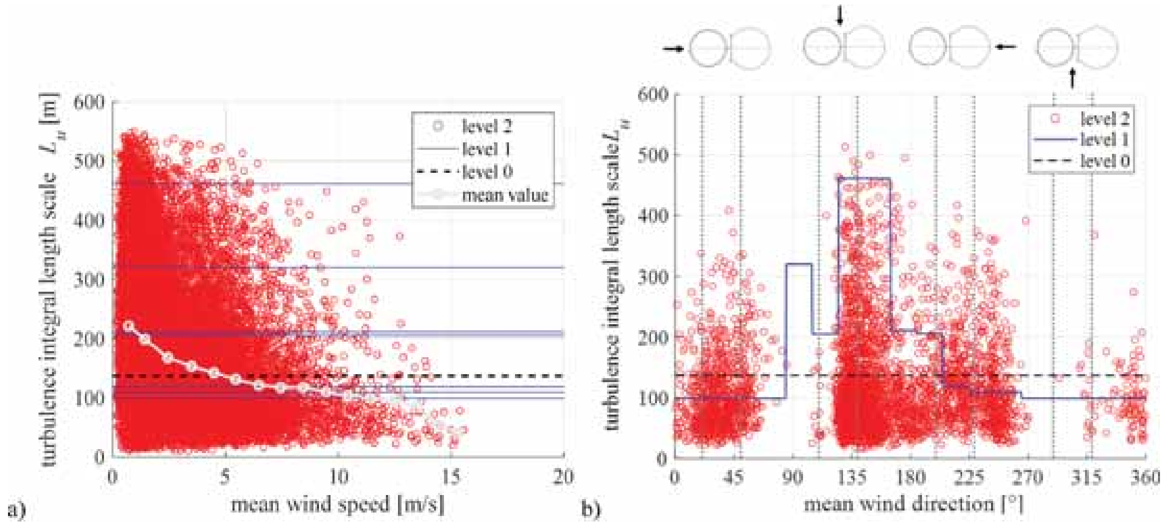

Fig. 9. Integral length scale of the longitudinal turbulence component at the anemometer height, evaluated with the three accuracy levels: a) versus mean wind velocity; b) versus mean wind direction.

lines), which are capable of capturing the effect of directional roughness under neutral atmospheric conditions. Nevertheless, the Level 1 calculation tends to underestimate the measured values of I_u and overestimate L_u for winds originating from the second quadrant, centered around 135° (β = 90–180°). This sector corresponds to sea winds (Fig. 2), for which the CNR-DT guidelines prescribe a very small roughness length, z_0 = 0.002 m. Since the structure under investigation is located within a bay, the effective roughness may be higher than the prescribed open-sea value. In this context, the surrounding topography should be regarded as an inherent characteristic of the bay setting, directly shaping the wind field and thus contributing to the discrepancy between measured and estimated turbulence intensity. In contrast, Level 0 provides a constant estimate that roughly averages the whole data.

6.2. Aerodynamic coefficients

Steel structures such as poles and monotubular towers typically consist of slender polygonal shafts with more than 12 sides. These often incorporates longitudinal elements, such as weld beads, ducts, and ladders, for which wind tunnel tests remain scarce and offer limited benchmarks. To address this gap, a dedicated wind tunnel test campaign was carried out in the Giovanni Solari Boundary Layer Wind Tunnel at the Genoa University. Tests were performed on a sectional model of a lighting pole, reproducing its 16-sided cross section with the attached ladder [84], as well as on a model of the top platform with lighting fixtures [60].

At Level 2, the drag coefficient of the column with the ladder is directly obtained from the experimental measurements. The red circles in Fig. 10 shows the values inferred from the wind tunnel measurements at the reference cross section of the pole under turbulent flow conditions, for wind directions aligned with the η- (a) and ζ-axis (b). These values are plotted against a corrected Reynolds number $f_T \times Re$, where f_T is a non-dimensional factor accounting for the effect of flow turbulence on C_D [85], and Re is the Reynolds number. The red line represents an interpolating function used to estimate the coefficient across the entire Re range of interest. Such extrapolation may introduce additional uncertainty due to the well-known Reynolds number sensitivity of many-sided cylinders (e.g., [86]). However, in the present evaluations, the Re values of interest remain within those tested in the wind tunnel, or at most within the pre-transcritical plateau region where the drag

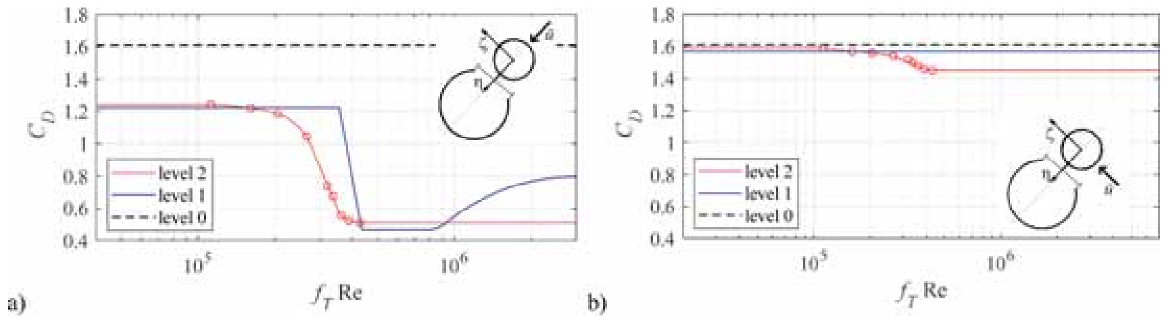

Fig. 10. Drag coefficient of the pole with the ladder; wind direction aligned with structural axis η (a) and ζ (b).

coefficient is expected to be approximately constant.

At Level 1, the ladder is characterized using CNR-DT 207, while the shaft is characterized using ESDU 79026, which provides the drag coefficient for different Reynolds regimes and turbulence conditions for sections up to 20 sides, treating a polygonal section as a circular section characterized by an equivalent roughness. As suggested by existing guidelines (e.g., [14]), the drag coefficient of the column-ladder assembly is obtained by summing the two contributions. The blue line in Fig. 10 represents this estimate.

At Level 0, both components, shaft and ladder, are characterised according to CNR-DT 207, adopting the highest coefficient as a conservative estimate, corresponding to wind aligned with the ζ axis. The dashed black line in Fig. 10 represents this estimate.

The comparison between these different lines shows a significant overestimation of C_D at Level 0, especially when the wind is aligned with the structural axis η, where the ladder lies in the shaft's wake.

Regarding the aerodynamic coefficients of the top platform, all accuracy levels adopt the values obtained from wind tunnel measurements [60], as reliable simplified estimation methods are not available for this unique configuration.

6.3. Dynamic structural parameters

The modal shapes and fundamental frequencies can be determined from finite element models. For relatively simple structures such as lighting poles, this approach is typically quite accurate when the geometry and structural details are well known. Nevertheless, some differences may occur when comparing numerical predictions with values obtained from in-situ measurements (e.g., [87]). These differences can arise from additional stiffness provided by non-structural elements, from flexibility at the base joint due ground-structure interaction or from specific structural detailing (e.g., [88]).

The finite element model of the investigated structure identifies two fundamental vibration modes along the principal structural inertia axes, corresponding to the first bending modes of the pole in the two orthogonal planes. The numerical results show good agreement with the outcomes of the dynamic identification obtained from ambient vibrations. Therefore, in the present study, the modal frequencies are taken as those identified from ambient measurements for all accuracy levels, namely, $n_{1\zeta} = 0.74$ Hz, $n_{1\eta} = 0.84$ Hz in the ζz and ηz plane, respectively. These frequencies may correspond to either the along-wind or cross-wind direction, depending on the prevailing wind. The modal shapes are determined from the numerical model and are well approximated by the following formula (with α=ζ, η)

$$\psi_{1\alpha}(z) = \left(\frac{z}{h}\right)^{a_\alpha} \tag{28}$$

with $a_\zeta = 1.77$, $a_\eta = 1.97$.

Damping is one of the most uncertain parameters in structural design, and its measurement and prediction remains a major challenge in structural dynamics. A recent investigation [89] has shown that uncertainties persist even in the simplified case of monotubular towers composed of bare steel columns and become more pronounced when lighting fixtures and ancillary components are added. The problem is further compounded by the difficulty of distinguishing between the structural and aerodynamic contributions.

At Level 2, the first modal damping ratio $\xi_{1\alpha}$, which includes both structural and aerodynamic components, is obtained from accelerometer signals using dynamic modal identification techniques based on the Enhanced Frequency Domain Decomposition (EFDD) method [90,91]. In Fig. 11 and Fig. 12, the red symbols show the estimated damping as a function of wind velocity, derived from 1-hour stationary acceleration time histories, with the wind coming from the 30° wide sector centered on the η- and ζ-axes. The empty dots represent values obtained from each time history, while the red filled dots indicate average values calculated within 1 m/s-wide wind velocity bins. At low wind velocities, when the aerodynamic contribution is negligible, the diagrams clearly show that structural dissipation is very small, even falling below 0.1%. As wind speed increases, aerodynamic damping progressively grows, particularly in the along-wind direction, which is also influenced by variations of the drag coefficient with Reynolds number.

At Level 1, structural damping is adopted from CNR-DT 207, which specifies a ratio of 0.2% for the fundamental mode of bare, unlined welded steel stacks; however, this value exceeds what observed in the diagram at low wind speed. Aerodynamic damping is computed using Eqs. (22), (23) of the analytical model [41]. The blue lines in Fig. 11 and Fig. 12 represent the sum of these two contributions, showing that the analytical estimates are able to reproduce the increase with wind speed with satisfactory accuracy, especially in the along-wind direction aligned with η (i.e., $\xi_{1\eta}$).

At accuracy Level 0, both structural and aerodynamic damping are derived from CNR-DT 207. In this case, the total damping, shown by black dotted lines, does not account for the contribution of equipment and ancillary components and therefore significantly underestimates the aerodynamic contribution.

The results emphasize the crucial role of aerodynamic damping for slender structures, which is an order of magnitude larger than the nearly negligible structural damping. The advanced analytical model at Level 1 can capture the complex aerodynamic effects of the shaft and localized masses, while the basic models at Level 0 fail to do so, leading to a significant underestimation of total damping.

7. Structural displacement comparison and discussion

Structural displacements from full-scale measurements under stationary wind events aligned with the structural principal axes are estimated using Eqs. (10)-(12), and compared with analytical model predictions, Eqs. (13)-(23), to assess the model's ability to capture the dynamic response and to quantify uncertainties arising from both the analytical formulation and the estimation of model parameters.

In Section 7.1, the structural response in terms of mean and maximum displacement is computed using the analytical model with

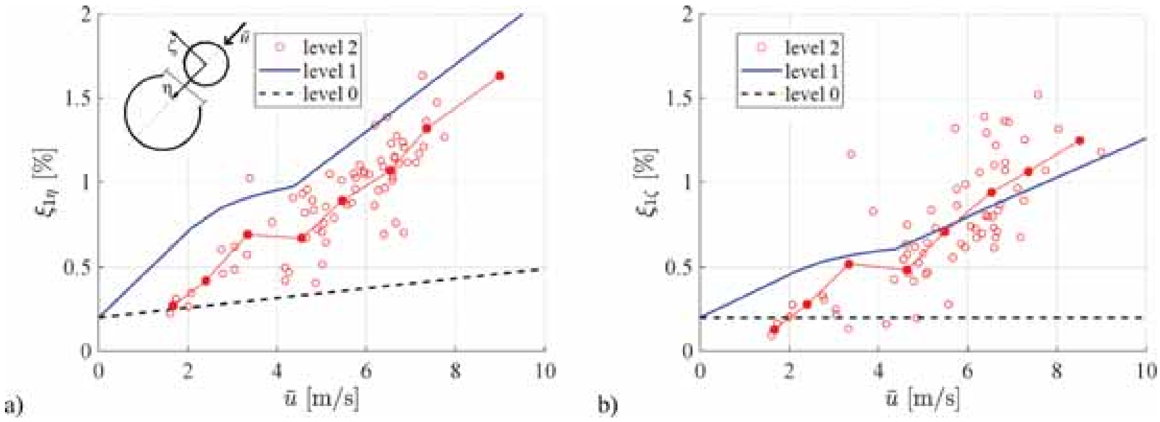

Fig. 11. Modal damping evaluated using the three accuracy levels for wind along η: a) along-wind, b) cross-wind.

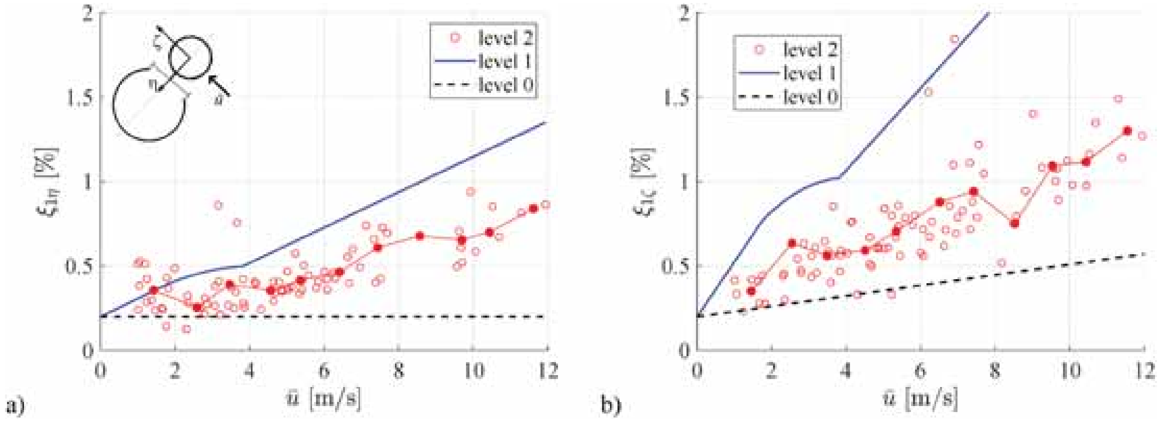

Fig. 12. Modal damping evaluated using the three accuracy levels for wind along ζ: a) cross-wind and b) along-wind.

Level 2 parameter estimates and compared with the full-scale response. Under the assumption that measurement errors are minor compared with other uncertainties, the discrepancies between the estimated and measured response is mainly attributed to the response-calculation model. In Section 7.2, the structural response is calculated using the analytical model with both Level 1 and Level 0 parameters. The increase in discrepancies between analytical and full scale response provides a basis for quantifying the contribution of uncertainties associated with parameter estimation. Section 7.3 narrows the scope to a reduced set of parameters, specifically turbulence intensity, the pole's drag coefficient, and damping, which were selected based on the observed dispersion and their established relevance in previous studies [81,92,93]. The selected parameters are assumed to be independent, and compensating effects from their interdependence are expected to be negligible.

To assess the contribution of each parameter's estimation uncertainty, a sensitivity analysis is carried out by treating them one at a time: for the parameter under consideration, the Level 1 (or Level 0) estimate is used, while all others are fixed at their Level 2. The procedure is then repeated for each parameter in the set. Assuming that Level 2 provides reliable estimates, any additional discrepancies between the measured and predicted response are interpreted as primarily associated with the parameter under investigation.

The comparison is performed in terms of 10-min mean and maximum top displacement of the tower, presented as functions of the mean wind velocity. Consistently with fundamental hypotheses of the calculation model, $N = 1973$ records of the wind speed and structural response are selected in which (i) wind speed and direction are stationary over 10-min intervals and (ii) the mean wind direction falls within a $\pm 15^\circ$ angular sector centered on the principal structural axes, η and ζ.

Using the displacement database derived from measurements through Eqs.(10) and (12), wind velocities are divided into 1-m/s bins and, for each i-th bin, the average measured value, A_i, is calculated. The percentage error (PE) is evaluated as:

$$PE_i = \frac{F_i - A_i}{A_i} \cdot 100 \tag{29}$$

where F_i is the displacement predicted by the analytical model. The mean absolute percentage error (MAPE) provides a global measure of the error magnitude over the entire velocity range:

$$\mathrm{MAPE} = \frac{1}{N} \sum_{i=1}^{N} |PE_i| \cdot 100 \tag{30}$$

Since MAPE does not convey information on the direction of the error (i.e., overestimation or underestimation), the mean percentage error (MPE) is also evaluated:

$$\mathrm{MPE} = \frac{1}{N} \sum_{i=1}^{N} PE_i \cdot 100 \tag{31}$$

To limit the influence of measurement noise at low wind speeds, both MAPE and MPE are computed only for velocity bins exceeding 3 m/s. As shown in the following sections, MAPE and MPE take very similar values, indicating the error is dominantly systematic; therefore, only MAPE is generally discussed.

7.1. Model errors

Fig. 13 shows the mean along-wind displacement for wind direction aligned with the η (a) and ζ axis (b) obtained from measurements (red

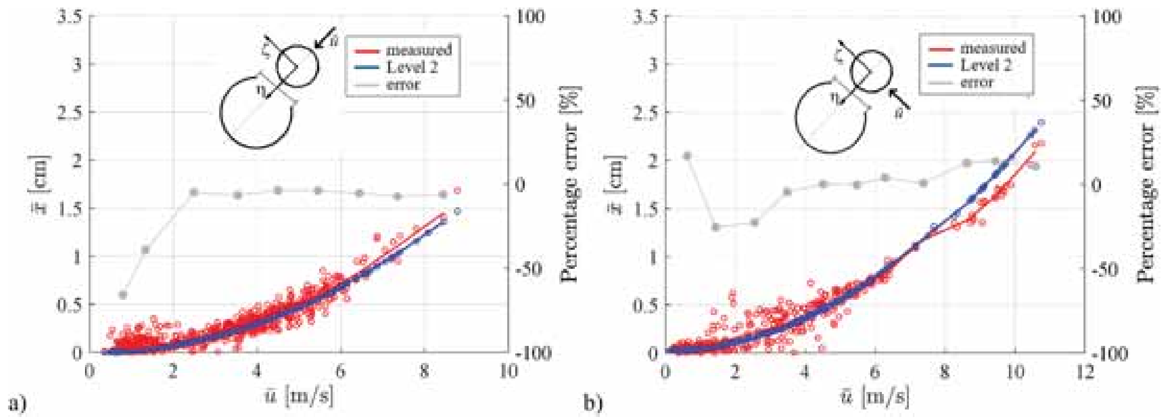

Fig. 13. Comparison of along-wind mean displacement evaluated at Level 2; wind along η, MAPE= 5%, MPE= -3% (a); along ζ, MAPE= 6%, MPE= 4% (b).

symbols; red line is the average) and from the calculation model with accuracy Level 2 parameters (blue symbols; blue line is the average). Grey symbols and lines indicate the percentage error (Eq. (29). Reynolds number is $Re \approx 3 \times 10^5$ at the highest wind speed. In this calculation, wind velocities below 2 m/s are excluded, as they are too low to be significant. The results demonstrate a very good agreement between experimental measurements and analytical predictions. The resulting MAPE is 5% for the η direction and 6% for the ζ direction.

Fig. 14 and Fig. 15 present maximum along-wind and cross-wind displacements. Some increased variability is observed, with greater discrepancies in the cross-wind direction. The measured values generally fall below model prediction, indicating that, in the investigated case, the calculation model tends to be overconservative. This discrepancy appears to support the presence of a systematic overestimation of the maximum displacement by the analytical model. It should be noted, however, that direct displacement measurements were not available, and the uncertainty associated with the reconstructed displacement could not be quantitatively assessed.

MAPE values are 44% (η) and 7% (ζ) for the along-wind displacement, and 111% (η) and 64% (ζ) for the cross-wind displacement. Vortex shedding effects are expected to be negligible, as the critical wind speed resonant with the first vibration mode is below 2 m/s.

Table 2 summarizes the MAPE values for these cases (row labeled 'Level 2').

7.2. Errors associated with parameter estimates

Fig. 16, Fig. 17, Fig. 18 present the mean along-wind, maximum along-wind and maximum cross-wind displacement for wind direction aligned with η. Analytical estimates (blue) are obtained from the calculation model using accuracy Level 1 parameters (panels a) and Level 0 parameters (panels b). Measurement-based displacements are shown in red, while the percentage error per velocity bin is shown in grey. Table 2 reports the complete report in terms of MAPE values for wind direction along η and ζ (rows labeled 'Level 1' and 'Level 0').

For the along-wind mean displacement, Level 1 predictions (Fig. 16a) closely match the measured values, showing a slight underestimation, with a MAPE of 7%. In contrast, using Level 0 parameters (Fig. 16b) systematically overestimates the structural response, resulting in a much higher MAPE of 94%.

When considering the maximum response, minor discrepancies appear in the along-wind directions (Fig. 17), while larger deviations are observed in the cross-wind direction (Fig. 18). Level 1 estimations (panels a) are conservative, with a MAPE very similar to that of Level 2. This is due, on the one hand, to the accuracy of the parameter estimates, and, on the other hand, to compensating effects between over- and underestimation. By contrast, the Level 0 results (panels b) show pronounced overestimations, with MAPE values up to four times higher than those obtained with Level 1 parameters. This outcome reflects the safety-oriented principles of the guidelines, where conservative assumptions accumulate and ultimately lead to substantially overestimated responses.

7.3. Errors connected to single parameters

The effects of errors connected to turbulence intensity, drag coefficient, and damping estimates are analyzed, considering each of them singularly.

The error introduced in the response estimation due to the assessment of turbulence intensity is investigated by comparing the along-

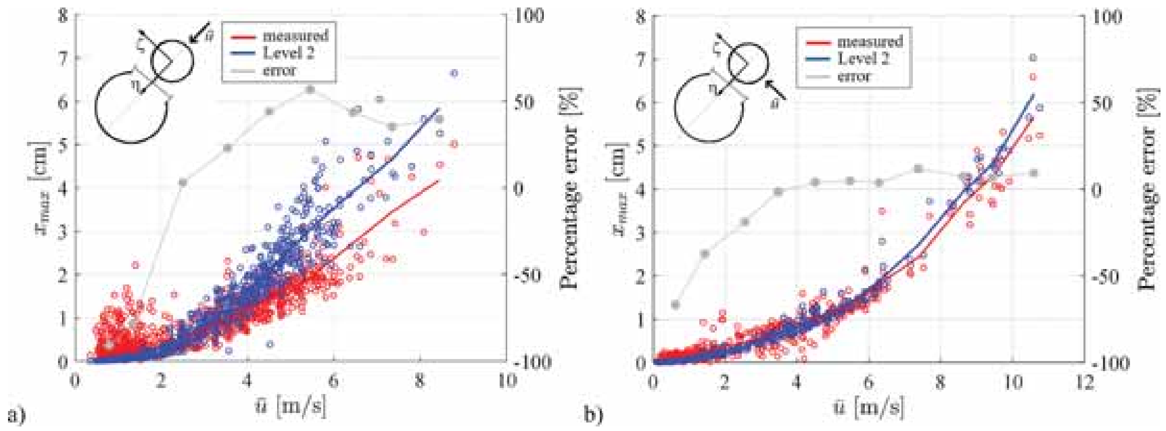

Fig. 14. Comparison of along-wind maximum displacement evaluated at Level 2; wind along η, MAPE= 44%, MPE= 44% (a), along ζ, MAPE= 7%, MPE= 5% (b).

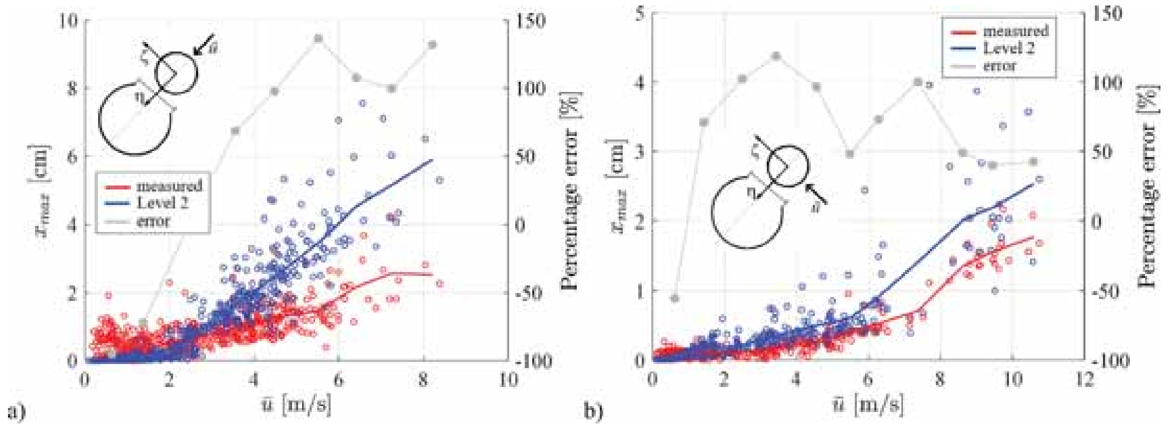

Fig. 15. Comparison of cross-wind maximum displacement evaluated at Level 2; wind along η, MAPE= 111%, MPE= 111% (a), along ζ, MAPE= 64%, MPE= 64% (b).

Table 2
MAPE of the displacement calculation at Level 2, 1 and 0.

accuracy level	along-wind mean (η)	along-wind mean (ζ)	along-wind max (η)	along-wind max (ζ)	cross-wind max (η)	cross-wind max (ζ)
Level 2	5%	6%	44%	7%	111%	64%
Level 1	7%	9%	38%	36%	117%	19%
Level 0	94%	15%	115%	92%	457%	160%

wind maximum response obtained from measurements with the response computed by assuming I_u from the Level 1 and Level 0 approaches, while all other parameters are estimated at Level 2. Fig. 19 and Fig. 20 present these comparisons for wind directions aligned with the η and ξ axes, respectively, showing results obtained using Level 1 (panel a) and Level 0 (panel b). Table 3 reports the MAPE values.

Despite the significant dispersion of I_u that was observed in Fig. 8, when the wind direction is aligned with η (Fig. 8b, sectors at 45° and 225° from North) the Level 1 estimation of this quantity provides a reasonably accurate and conservative prediction. In contrast, the Level 0 slightly underestimates I_u. As a result, the along-wind maximum response predicted by the analytical model at Level 1 (Fig. 19a) yields a MAPE of 59%, slightly higher than that obtained at Level 2 (Fig. 14a), yet remaining on the conservative side. At Level 0 (Fig. 19b), the calculated response is closer to the measured values, with a MAPE of 4%, which is lower with respect to Level 1, but slightly non-conservative.

When the wind is aligned with ζ, the opposite trend is observed: the Level 1 approach slightly underestimates I_u compared with Level 0, especially in the most populated sector (Fig. 8b, sector at 135° from North). Consequently, the analytical response calculated with turbulence intensity at Level 1 reduces the overestimation provided by the model, achieving a MAPE 2% (that is lower than that of Level 2), still remaining on the conservative side (Fig. 20a). The reduction is less pronounced for Level 0 (Fig. 20b), which yields a MAPE of 34%, though still conservative.

It is worth highlighting that, due to the large variability in full-scale turbulence intensity measurements, directional estimates at Level 1 rarely provide highly accurate predictions of I_u Nonetheless, they consistently yield conservative, safe-side results. In contrast, simplified, non-directional approaches may underestimate I_u, potentially resulting in non-conservative and unsafe outcomes.

The role of the drag coefficient is investigated comparing the along-wind mean response obtained from measurements with the response computed using C_D from the Level 1 and Level 0 estimates, while all other parameters are taken from Level 2 estimates. Fig. 21 and Fig. 22 show the comparison for wind aligned with η and ζ obtained using Level 1 (panel a) and Level 0 (panel b). Table 4 summarizes the results in terms of MAPE.

When wind is aligned with η, the estimate of the drag coefficient at Level 1 is accurate, while it is largely overestimated at Level 0 (Fig. 10a), especially at high Reynolds number. Consequently, the mean response obtained by the analytical model at Level 1 (Fig. 21a) is very accurate and close to the estimate from measurements, with a MAPE of 7% very similar to that of Level 2, while it overestimates the measures at Level 0,

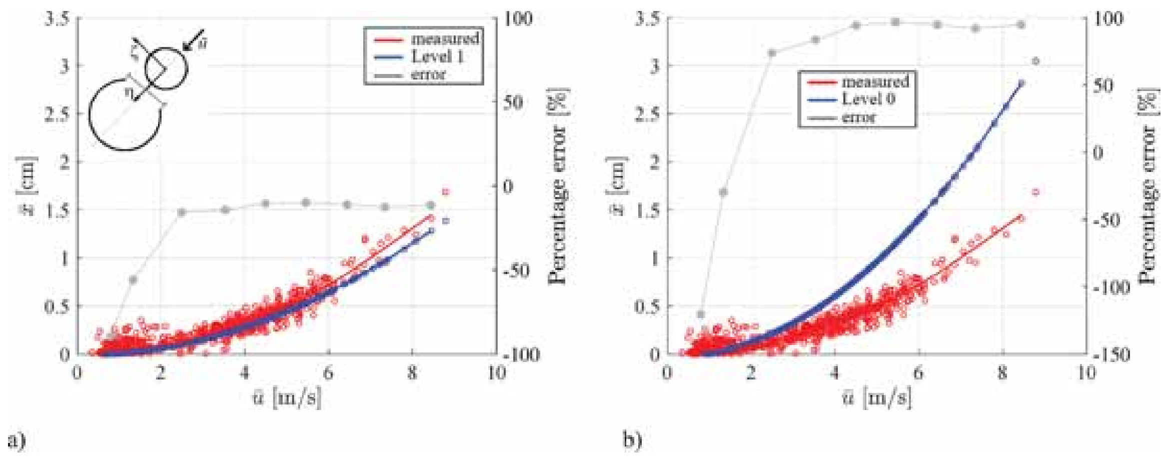

Fig. 16. Comparison of along-wind mean displacement for wind along η and parameters estimated at a) Level 1, MAPE= 7%, MPE= -7%, b) Level 0, MAPE= 94%, MPE= 94%.

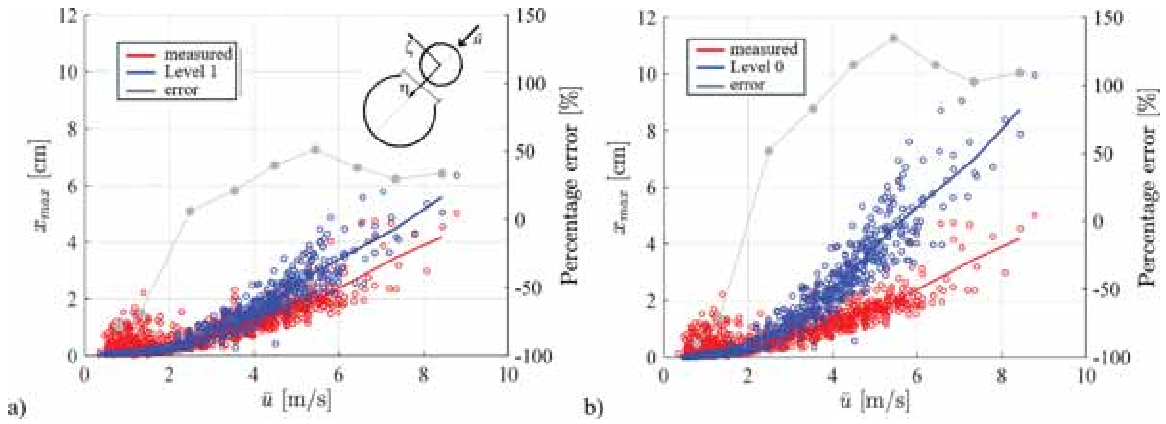

Fig. 17. Comparison of along-wind maximum displacement for wind along η and parameters estimated at a) Level 1, MAPE= 38%, MPE= 36%; b) Level 0, MAPE= 115%, MPE= 115%.

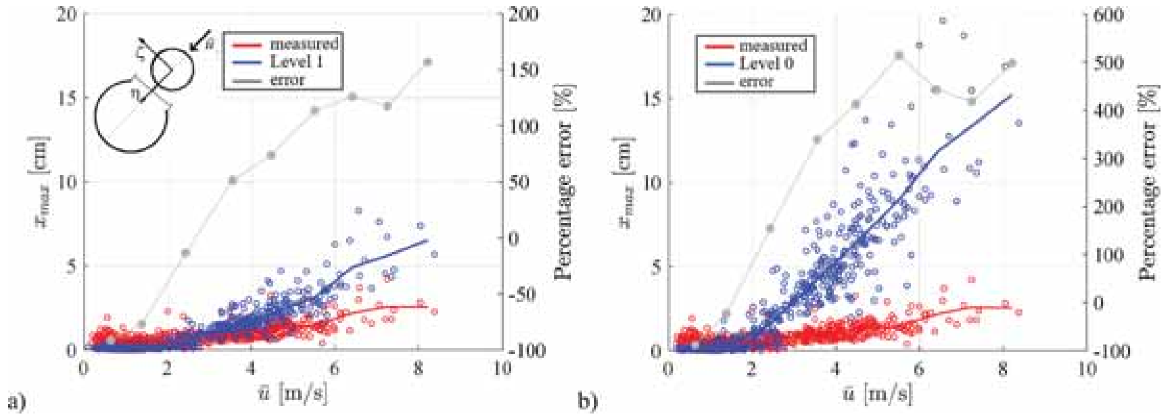

Fig. 18. Comparison of cross-wind maximum displacement for wind along η and parameters estimated at a) Level 1, MAPE= 117%, MPE= 117%; b) Level 0, MAPE= 457%, MPE= 457%.

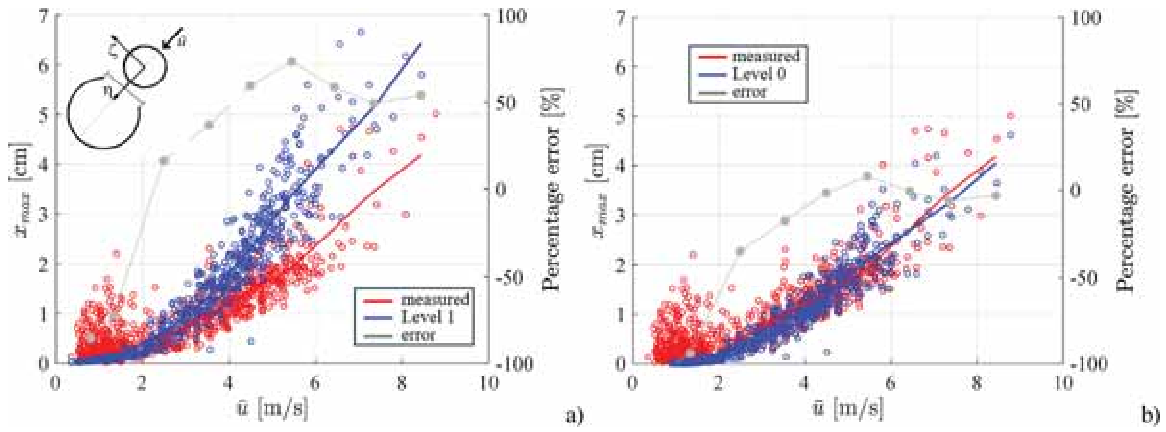

Fig. 19. Along-wind maximum displacement for wind along η, turbulence intensity estimated at a) Level 1, MAPE= 59%, MPE= 59%; b) Level 0, MAPE= 4%, MPE= -2%; all other parameters are estimated at Level 2.

with a MAPE of 117% (Fig. 21b). Conversely, when wind is aligned with ζ, the Levels 1 and 0 estimates of C_D are quite close, and in agreement with those at Level 2 (Fig. 10b). Consequently, the mean response obtained by the analytical model is fairly accurate at Level 1 and Level 0, with MAPEs of 8% and 10%, respectively, that are quite close to the MAPE at Level 2. This result shows that inaccuracies in the estimation of the drag coefficient play a dominant role in shaping the uncertainty pattern observed in the computation of the mean response and highlights the importance of properly accounting for the effect of ancillary components on the aerodynamic coefficient evaluation.

The role of damping estimate is investigated in the maximum along-wind (Fig. 23) and cross-wind displacements (Fig. 24) with the same procedure; results are presented limitedly to the wind speed aligned with η.

Table 5 reports the MAPE values.

Level 1 damping estimates are in close agreement with values

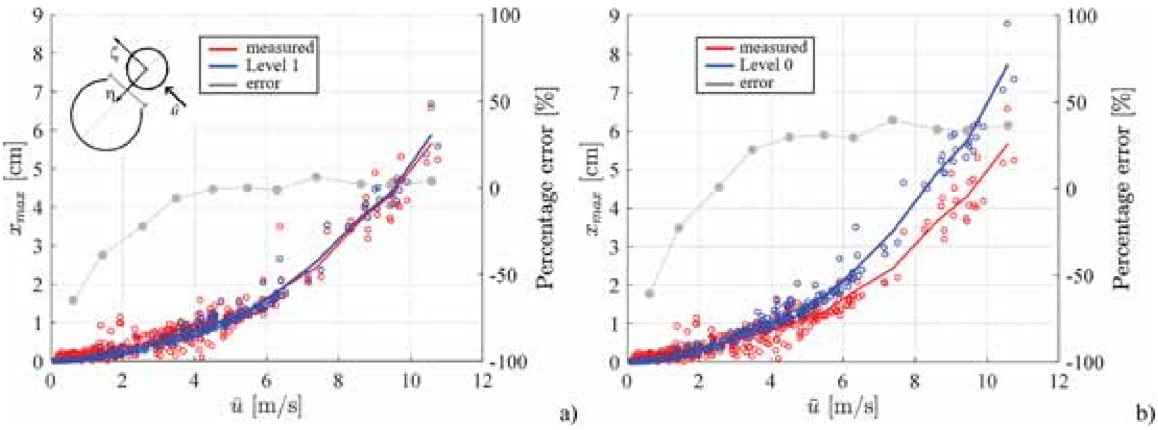

Fig. 20. Along-wind maximum displacement for wind along ζ, turbulence intensity estimated at a) Level 1, MAPE= 2%, MPE= 1%; b) at Level 0, MAPE= 34%, MPE= 34%; all other parameters are estimated at Level 2.

Table 3
MAPE with I_u estimated at Level 1 or 0; all other parameters are estimated at Level 2.

parameter estimation	along-wind max (η)	along-wind max (ζ)
all at Level 2	44%	7%
I_u at Level 1	59%	4%
I_u at Level 0	2%	34%

obtained from measurements, both for the along-wind (Fig. 11a) and cross-wind directions (Fig. 11b). In contrast, the Level 0 approach does not adequately capture the aerodynamic contribution, leading to substantial underestimations of this parameter. Therefore, the Level 1 prediction of the maximum response shown in Fig. 23a and Fig. 24a is quite accurate, with MAPE values of 30% and 113%, respectively, comparable to those obtained at Level 2 (Fig. 14a and Fig. 15a) and consistently on the safe side. Conversely, the Level 0 calculation strongly overestimates the along-wind response (Fig. 23b), and even more

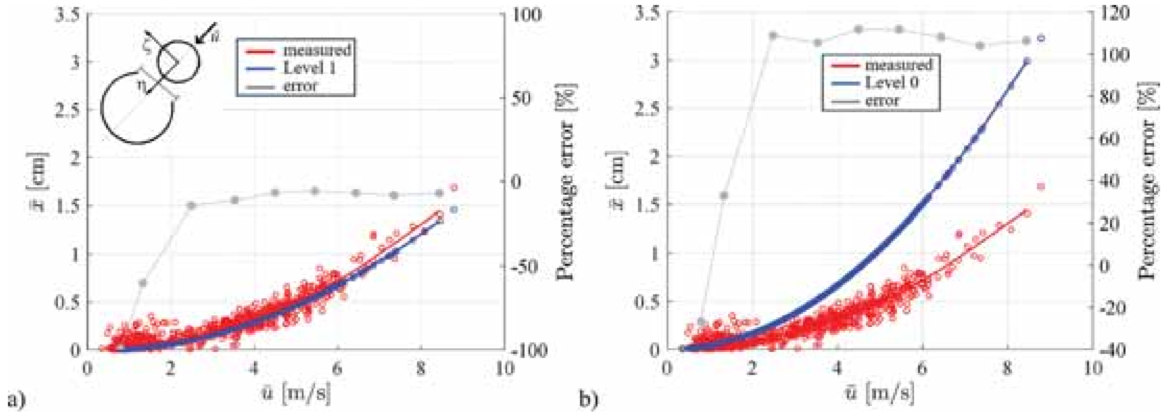

Fig. 21. Along-wind mean displacement for wind along η, drag coefficient estimated at a) Level 1, MAPE= 7%, MPE= -7%; b) Level 0, MAPE= 117%, MPE= 117%; all other parameters are estimated at Level 2.

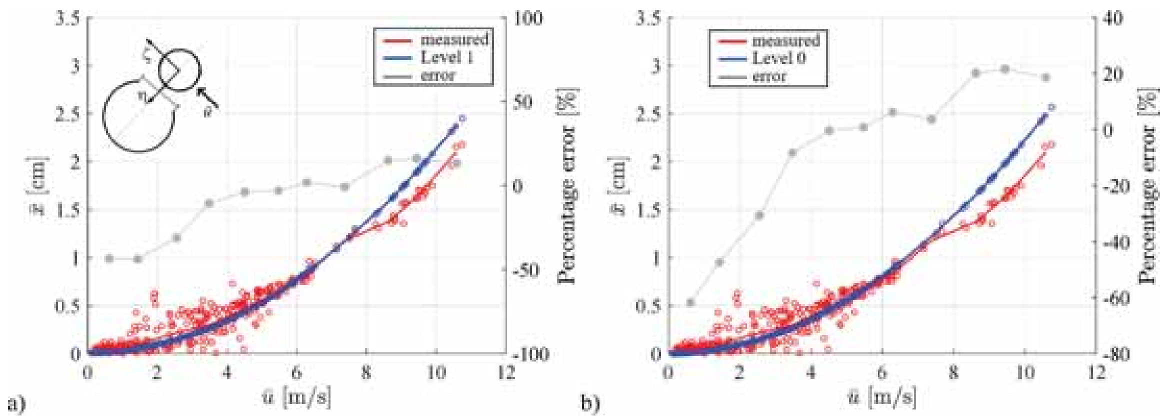

Fig. 22. Along-wind mean displacement for wind along ζ, drag coefficient estimated at: a) Level 1, MAPE= 8%, MPE= 6%; b) Level 0, MAPE= 10%, MPE= 8%; all other parameters are estimated at Level 2.

Table 4
MAPE with C_D estimated at Level 1 or 0; all other parameters are estimated at Level 2.

parameter estimation	along-wind mean (η)	along-wind mean (ζ)
all at level 2	5%	6%
C_D at Level 1	7%	8%
C_D at Level 0	117%	10%

markedly the cross-wind response (Fig. 24b), especially at high wind velocities, resulting in very high MAPE values of 188% and 350%, respectively.

The present findings confirm the critical role of aerodynamic damping in the dynamic response of slender structures. The use of prediction models that properly account for the aerodynamic dissipation of ancillary components markedly reduces uncertainty and provides more reliable response estimates.

8. Conclusions

This paper presents an experimental and analytical investigation of the wind-induced response of a slender steel lighting tower located in complex terrain, with emphasis on defining analysis levels that reflect practical engineering approaches and on quantifying the resulting errors. The key contributions of this research are (i) the long-term full-scale monitoring data of the slender monopole including complex ancillary components, under real environmental conditions; (ii) the combined use of strain- and acceleration-based techniques for displacement estimation; (iii) the quantification of parameter uncertainties using a three-level framework, namely site-specific measurements and refined analyses (Level 2), advanced analytical methods (Level 1), and simplified code-based approaches (Level 0); and (iv) the explicit separation and quantification of model bias versus parameter bias in the dynamic response analytical estimation.

The main findings of the study can be summarized as follows.

- The presented experimental campaign produced over 5000 h of high sampling rate measurements, including simultaneous wind velocity, strain, and acceleration data.
- The proposed data fusion technique enabled the derivation of an equivalent number of full-scale displacement records, providing a robust benchmark for analytical and numerical assessment of the dynamic response of slender structures.

Table 5
MAPE with ξ_α estimated at Level 1 or 0; all other parameters are estimated at Level 2.

parameter estimation	along-wind max (η)	cross-wind max (η)
all at level 2	44%	111%
ξ_α at Level 1	30%	113%
ξ_α at Level 0	188%	350%

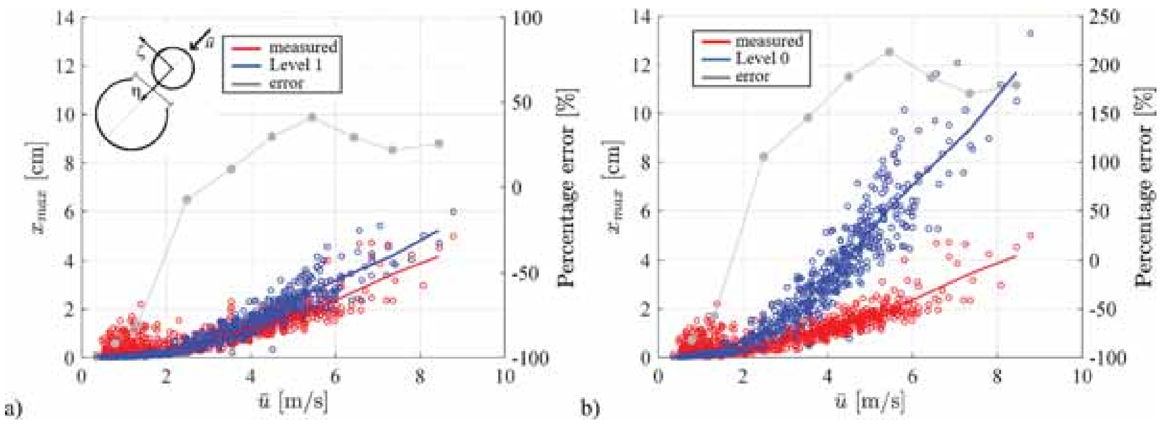

Fig. 23. Along-wind maximum displacement for wind along η, damping estimated at: (a) Level 1, MAPE= 30%, MPE= 30%; b) Level 0, MAPE= 188%, MPE= 188%; all other parameters are estimated at Level 2.

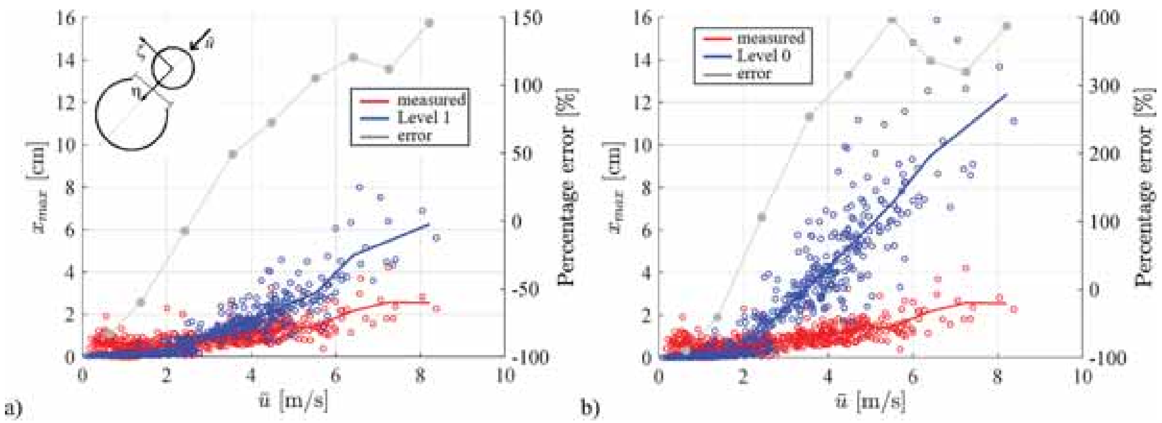

Fig. 24. Cross-wind maximum displacement for wind along η. Damping estimated at: (a) Level 1, MAPE= 113%, MPE= 113%; b) Level 0, MAPE= 350%, MPE= 350%; all other parameters are estimated at Level 2.

- Full-scale measured data, complemented by wind tunnel data [60, 84] were used to analyse wind, aerodynamic and dynamic parameters and the uncertainties associated with their estimation.
- Parameter values directly derived from the measurements (Level 2) exhibit significant dispersion. In particular, turbulence parameters show large variability on varying the mean wind velocity and direction, due to the thermal and shear effects. As the mean wind velocity increases, atmospheric conditions approach neutrality and the values align more closely, while still reflecting the directional effect of surface roughness. Aerodynamic parameters show strong Reynolds number effects, especially when ancillary components are in the wake. Damping exhibits a negligible structural component and a very large aerodynamic component, which increases nonlinearly with wind velocity.
- The advanced analytical methods (Level 1) estimate the model parameters with reasonable accuracy, in particular they capture the effect of local roughness on turbulence directional estimates under neutral atmospheric conditions; provide an acceptable approximation of aerodynamic drag coefficients over the relevant Reynolds number range; are capable of representing the complex aerodynamic effect of the shaft and localized masses in the damping estimation.
- The simplified code-based approaches (Level 0) generally estimate the selected parameters conservatively. In particular, they provide a constant estimate of roughness for turbulence estimation that roughly averages the entire data set, resulting with over- and underestimations; provide constant values of the drag coefficient, largely overestimated especially when ancillaries are in the wake of the pole; furnish overestimation of structural and large underestimation of aerodynamic damping components, failing to capture the crucial aerodynamic effect of localized masses and ancillaries.
- The analytical model for predicting the dynamic response of poles and monotubular towers, proposed by Solari and Pagnini [41], was used; it accounts for aerodynamic and aeroelastic effects arising from localized masses. The study further provided a validation and assessment of this model, clearly distinguishing between uncertainties arising from the model itself and those related to parameter estimation.
- When input parameters are derived from site measurements (Level 2), the displacements predicted by the analytical response model show good overall agreement with full-scale data. The model closely captures the mean response, provides good correspondence for the maximum along-wind displacement, and exhibits somewhat larger deviations in the cross-wind component. At high wind speeds, it systematically yields slightly conservative estimates, a desirable feature for engineering design.
- When the input parameters are predicted by accurate formulas (Level 1), the mean response provided by the analytical model remains in excellent agreement with full-scale measurements. Discrepancies in the maximum displacements are moderate in the along-wind response and more pronounced in the cross-wind direction. Predictions remain conservative, and the associated errors are in some cases comparable to those obtained using measured parameters. This indicates that the accurate parameter prediction is effective, while also revealing compensating effects between over- and underestimations.
- When the input parameters are estimated using code-based formulae (Level 0), the calculated response shows substantial overestimation, reflecting the safety-oriented nature of current guidelines, where conservative assumptions accumulate and result in conservatively high response predictions.
- The impact of parameter uncertainty on the dynamic response assessment was evaluated by varying individually turbulence intensity, aerodynamic coefficients, and damping across the different accuracy levels. Among these, the contribution of ancillary components to the drag coefficient and aerodynamic damping emerged as the dominant source of uncertainty. In particular, the use of code-prescribed damping values leads to marked overestimation in the case analyzed. This underscores the importance of accurately capturing the aerodynamic contribution to damping in the gust-excited response, while the structural contribution plays a key role in vortex-induced vibrations ([94], [95])

The findings reinforce the importance of full-scale validation studies, complementing research on high-rise buildings, long-span bridges, and monotubular towers.

Future research should directly validate the proposed data fusion approach using additional instrumentation capable of measuring displacement (e.g., vision-based techniques). Further studies should also extend the proposed methodology to other classes of slender structures susceptible to vortex-induced vibrations, investigate non-stationary wind phenomena such as thunderstorm downbursts, and examine in more detail the role of aerodynamic damping in the presence of localized masses. These developments will enhance the reliability of simplified engineering models and support safer, more serviceable, and more resilient wind-resistant design practices.

CRediT authorship contribution statement

Maria Pia Repetto: Writing – review & editing, Validation, Supervision, Methodology, Funding acquisition, Conceptualization. **Luisa Pagnini:** Writing – review & editing, Validation, Supervision, Methodology, Conceptualization. **Andrea Orlando:** Writing – original draft, Validation, Software, Methodology, Investigation, Formal analysis, Data curation, Conceptualization.

Declaration of Competing Interest

The authors declare that they have no known competing financial interests or personal relationships that could have appeared to influence the work reported in this paper.

Acknowledgements

The first and third authors acknowledge the support by the European Union - NextGenerationEU and by the Ministry of University and Research (MUR), National Recovery and Resilience Plan (NRRP), Mission 4, Component 2, Investment 1.5, Project “RAISE - Robotics and AI for Socio-economic Empowerment” (ECS00000035).

Data availability

Data will be made available on request.

References

[1] Davenport AG. The spectrum of horizontal gustiness near the ground in high winds. Quart J R Meteor Soc 1961;87:194–211. https://doi.org/10.1002/qj.49708737208.
[2] Davenport AG. Note on the distribution of tile largest value of a random function with application to gust loading. Proc Inst Civ Eng 1964;28(2):187–96. https://doi.org/10.1680/iicep.1964.10112.
[3] Davenport AG. Gust loading factors. J Struct Div ASCE 1967;93(3). https://doi.org/10.1061/JSDEAG.0001692.
[4] ECCS. Recommendations for the calculation of wind effects on buildings and structures. Eur Conv Constr Steel Bruss 1978.
[5] ESDU 76001 1976. The response of flexible structures to atmospheric turbulence. London, UK.
[6] Holmes JD. Along-wind response of lattice towers: Part I derivation of expressions for gust response factors. Eng Struct 1994;16:287–92. https://doi.org/10.1016/0141-0296(94)90069-8.
[7] Kasperski M, Niemann H-J. The LRC (Load-response-correlation) method: A general method of estimating unfavourable wind load distributions for linear and nonlinear structural behaviour. J Wind Eng Ind Aerodyn 1992;43:1753–63. https://doi.org/10.1016/0167-6105(92)90588-2.
[8] Zhou Y, Kareem A. Gust loading factor: new model. J Struct Eng 2001;127(2):168–75. https://doi.org/10.1061/(ASCE)0733-9445(2001)127:2(168).

[9] Piccardo G, Solari G. Closed form prediction of 3-D wind-excited response of slender structures. J Wind Eng Ind Aerodyn 7476 1998:697–708. https://doi.org/10.1016/S0167-6105(98)00063-4.

[10] Piccardo G, Solari G. 3D wind-excited response of slender structures: Closed-form solution. J Struct Eng-ASCE 2000;126:936–43. https://doi.org/10.1061/(ASCE)0733-9445(2000)126:8(936).

[11] Piccardo G, Solari G. 3-D gust effect factor for slender vertical structures. Probab Eng Mech 2002;17:143–55. https://doi.org/10.1016/S0266-8920(01)00034-0.

[12] Repetto MP, Solari G. Equivalent static wind actions on vertical structures. J Wind Eng Ind Aerodyn 2004;92(5):335–57. https://doi.org/10.1016/j.jweia.2004.01.002.

[13] Pagnini LC, Piccardo G. A generalized gust factor technique for evaluating the wind–induced response of aeroelastic structures sensitive to vortex-induced vibrations. J Fluids Struct 2017;70:181–200. https://doi.org/10.1016/j.jfluidstructs.2017.01.017.

[14] CNR. Guide for the Assessment of Wind Actions and Effects on Structures. Rome: CNR-DT 207/2008. National Research Council of Italy; 2010.

[15] EN 1991-1-4. Eurocode 1: Actions on Structures – Part 1.4: General Actions – Wind Actions. CEN. Brussels, Belgium: European Commitee for Standardization; 2005.

[16] Caracoglia L., Jones N.P. 2006. Wind-Induced Failures of Highway Light Poles during Winter Storms. Proc. ASME 2006 Pressure Vessels and Piping/ICPVT-11 Conference, 9: 197-206, Vancouver, BC. https://doi.org/10.1115/PVP2006-ICPVT-11-93579.

[17] Caracoglia L, Jones NP. Numerical and experimental study of vibration mitigation for highway light poles. Eng Struct 2007;29(5):821–31. https://doi.org/10.1016/j.engstruct.2006.06.023.

[18] Repetto MP, Solari G. Wind-induced fatigue collapse of real slender structures. Eng Struct 2010;32:3888–98. https://doi.org/10.1016/j.engstruct.2010.09.002.

[19] Wang L., Fan X.Failure cases of high chimneys: A review. Failure cases of high chimneys: A review 105: 1107-1110. https://doi.org/10.1016/j.engfailanal.2019.07.0322019.

[20] Chen Y, Wang X, Sun C, Zhu B. Exploring the failure mechanism of light poles on elevated bridges under high winds. Eng Fail Anal 2024;159:108076. https://doi.org/10.1016/j.engfailanal.2024.108076.

[21] Lupi F, Höffer R, Niemann H-J. Aerodynamic damping in vortex resonance from aeroelastic wind tunnel tests on a stack. J Wind Eng Ind Aerodyn 2021;208:104438. https://doi.org/10.1016/j.jweia.2020.104438.

[22] Zhu Y, Chen F, Li Q. Aerodynamic loads of tapered tall buildings: Insights from wind tunnel test and CFD. Structures 2023;56:104975. https://doi.org/10.1016/j.istruc.2023.104975.

[23] Melaku AF, Bitsuamlak GT. Prospect of LES for predicting wind loads and responses of tall buildings: A validation study. J Wind Eng Ind Aerodyn 2024;244:105613. https://doi.org/10.1016/j.jweia.2023.105613.

[24] Eissa M, Ibrahim HA, Elawady A. Aeroelastic testing of monopole mounted on a high-rise building under atmospheric boundary layer wind. J Wind Eng Ind Aerodyn 2025;264:106149. https://doi.org/10.1016/j.jweia.2025.106149.

[25] Satake N, Suda K, Arakawa T, Sasaki A, Tamura Y. Damping Evaluation Using Full-Scale Data of Buildings in Japan. J Struct Eng-ASCE 2003;129(4):470–7. https://doi.org/10.1061/(ASCE)0733-9445(2003)129:4(470).

[26] Tamura Y. Amplitude dependency of damping in buildings and estimation techniques. Proc 12th Austral-Asian Wind Eng Soc Workshop Queenstown NZ 2006.

[27] Kijewski-Correa T, Kilpatrick J, Kareem A, Morrish D. Validating the wind-induced response of tall buildings: a synopsis of the Chicago Full-Scale Monitoring Program. J Struct Eng 2006;132(10):1509–23. https://doi.org/10.1061/(ASCE)0733-9445(2006)132:10(1509).

[28] Li Q, Xiao YQ, Fu JY, Li ZN. Full-scale measurements of wind effects on the Jin Mao building. J Wind Eng Ind Aerodyn 2007;95(6):445–66. https://doi.org/10.1016/j.jweia.2006.09.002.

[29] Fu JY, Wub JR, Xu A, Li Q, Xiao YQ. Full-scale measurements of wind effects on Guangzhou West Tower. Eng Struct 2012;35:120–39. https://doi.org/10.1016/j.engstruct.2011.10.022.

[30] He YC, Li Q. Dynamic responses of a 492-m-high tall building with active tuned mass damping system during a typhoon. Struct Control Health Monit 21 705720 2014. https://doi.org/10.1002/stc.1596.

[31] Li X, Li QS. Observations of typhoon effects on a high-rise building and verification of wind tunnel predictions. J Wind Eng Ind Aerodyn 2019;184:174–84. https://doi.org/10.1016/j.jweia.2018.11.026.

[32] Xu K, Li Q, Zhou K, Han X. Dynamic performance of a supertall building with an active tuned mass damper system during Super Typhoon Saola. Eng Struct 2024:118778. https://doi.org/10.1016/j.engstruct.2024.118778.

[33] Zhou Y, Sun L. Effects of high winds on a long-span sea-crossing bridge based on structural health monitoring. J Wind Eng Ind Aerodyn 2018;174:260–8. https://doi.org/10.1016/j.jweia.2018.01.001.

[34] Petersen ØW, Øiseth O, Lourens E. Investigation of dynamic wind loads on a long-span suspension bridge identified from measured acceleration data. J Wind Eng Ind Aerodyn 2020;196:104045. https://doi.org/10.1016/j.jweia.2019.104045.

[35] Andersen M, Isaksen B, Hansen S. Full-Scale Monitoring of the Wind Field, Surface Pressures and Structural Response of Gjemnessund Suspension Bridge. Struct Eng Int 2021;32:1–12. https://doi.org/10.1080/10168664.2021.1953426.

[36] Fenerci A, Kvåle KA, Petersen ØW, Rønnquist A, Øiseth O. Dataset from long-term wind and acceleration monitoring of the hardanger bridge. J Struct Eng 2021;147(5):04721003. https:// doi.org/10.1061/(ASCE)ST.1943-541X.0002997.

[37] Robertson AP, Hoxey RP, Short JL, Ko RHY. Wind-induced fatigue loading of tubular steel lighting columns. Wind Struct 2001;4(2):163–76. https://doi.org/10.12989/was.2001.4.2.163.

[38] Capilla JJA, Au SK, Brownjohn JMW, Hudson E. Ambient vibration testing and operational modal analysis of monopole telecoms structures. J Civ Struct Health Monit 2021;11:1077–91. https://doi.org/10.1007/s13349-021-00499-4.

[39] Romanic D, Shoji H, Hangan H. Experimental investigation of surface pressures, velocities, and dynamic structural analysis of tornadic winds on a luminary pole. J Fluid Struct 2023;116:103794. https://doi.org/10.1016/j.jfluidstructs.2022.103794.

[40] Ellingsen ØM, Flamand O, Amandolese X, Coiffet F, Hémon P. Field Tests on a Full-Scale Steel Chimney Subjected to Vortex-Induced Vibrations. Struct Eng Int 2022;32(1):55–61. https://doi.org/10.1080/10168664.2021.1936352.

[41] Solari G, Pagnini LC. Gust buffeting and aeroelastic behaviour of poles and monotubular towers. J Fluid Struct 1999;13(7-8):877–905. https://doi.org/10.1006/jfls.1999.0240.

[42] ASCE-SEI 7-16. Minimum Design Loads and Associated Criteria for Buildings and Other Structures. Reston: American Society of Civil Engineers; 2017.

[43] Simiu E, Yeo DH. Wind Effects on Structures: Modern Structural Design for Wind. John. Wiley & Sons Ltd; 2019. https://doi.org/10.1002/9781119375890.

[44] Nandi TN, Yeo DH. Estimation of integral length scales across the neutral atmospheric boundary layer depth: A Large Eddy Simulation study. J Wind Eng Ind Aerodyn 2021;218:104715. https://doi.org/10.1016/j.jweia.2021.104715.

[45] Solari G, Piccardo G. Probabilistic 3-D turbulence modeling for gust buffeting of structures. Probab Eng Mech 2001;16(1):73–86. https://doi.org/10.1016/S0266-8920(00)00010-2.

[46] von Kármán T. Progress in the statistical theory of turbulence. Proc Nat Acad Sci USA 1948;34:530–9.

[47] Kaimal JC, Wyngaard JC, Izumi Y, Coté OR. Spectral characteristics of surface-layer turbulence. Quart J R Meteor Soc 1972;98:563–89. https://doi.org/10.1002/qj.49709841707.

[48] Simiu E. Wind spectra and dynamic alongwind response. ASCE J Struct Div 1974;100(9):1897–910. https://doi.org/10.1061/JSDEAG.0003880.

[49] Harris R.I. 1968. 5273. On the spectrum and auto-correlation function of gustiness in high winds. ERA Report 5273.

[50] Harris RI. Some further thoughts on the spectrum of gustiness in strong winds. J Wind Eng Ind Aerodyn 1990;33(3):461–77. https://doi.org/10.1016/0167-6105(90)90001-S.

[51] Højstrup J. A simple model for the adjustment of velocity spectra in unstable conditions downstream of an abrupt change in roughness and heat flux. Bound Lay Meteor 1981;21(3):341–56. https://doi.org/10.1007/BF00119278.

[52] Berman S., Stearns C.R. 1977. Near-earth turbulence and coherence measurements at Aberdeen proving ground. Bound Lay Meteorol 11: 485-506. https://doi.org/10.1007/BF02185872.

[53] Deaves DM, Harris RI. A mathematical model of the structure of strong winds. CIRIA Report 76. London: Construction Industry Research and Information Association; 1978.

[54] Mann J. The spatial structure of neutral atmospheric surface-layer turbulence. J Fluid Mech 1994;273:141–68. https://doi.org/10.1017/S0022112094001886.

[55] Krenk S. Wind field coherence and dynamic wind forces. In: Naess A, Krenk S, editors. IUTAM Symposium on Advances in Nonlinear Stochastic Mechanics; 1996 (Kluwer, Dordrecht).

[56] Kristensen L, Jensen NO. Lateral coherence in isotropic turbulence and in the natural wind. Bound Lay Meteor 1979;17(3):353–73. https://doi.org/10.1007/BF00117924.

[57] Cheynet E, Jakobsen JB, Reuder J. Velocity Spectra and Coherence Estimates in the Marine Atmospheric Boundary Layer. Bound Lay Meteor 2018;169:429–60. https://doi.org/10.1007/s10546-018-0382-2.

[58] ESDU 86010 1991. Characteristics of atmospheric turbulence near the ground. Part III: Variation in space and time for strong winds (neutral atmosphere), London, UK.

[59] Orlando A. 2021. Full-scale monitoring of the wind-Induced response of vertical slender structures, with fixed and rotating masses (Ph.D. thesis). University of Genoa.

[60] Mengistu MT, Orlando A, Repetto MP. Wind and structural response monitoring of a lighting pole for the study of downburst effects on structures. J Wind Eng Ind Aerodyn 2023;240:105447. https://doi.org/10.1016/j.jweia.2023.105447.

[61] Mengistu MT, Repetto MP. Analytical downburst wind load calculation methods: Review and full-scale validation. Eng Struct 2024;321:118970. https://doi.org/10.1016/j.engstruct.2024.118970.

[62] Wu R-T, Jahanshahi MR. Data fusion approaches for structural health monitoring and system identification: Past, present, and future. Struct Health Monit 2020;19(2):552–86. https://doi.org/10.1177/1475921718798769.

[63] Kochly M. Validation of Global Positioning Systems for Monitoring Civil Infrastructure Systems: Performance Assessment and Removal of Multipath Effects. Dept of Civil Engineering and Geological Sciences, Notre Dame, IN, University of Notre Dame; 2006.

[64] Park JW, Sim SH, Jung HJ. Displacement estimation using multimetric data fusion. IEEE ASME Trans Mechatron 2013;18(6):1675–82. https://doi.org/10.1109/TMECH.2013.2275187.

[65] Ma Z, Chung J, Liu P, Sohn H. Bridge displacement estimation by fusing accelerometer and strain gauge measurements. Struct Control Health Monit 2021;28(6):e2733. https://doi.org/10.1002/stc.2733.

[66] Zhu H, Gao K, Xia Y, Hu Q. Multi-rate data fusion for dynamic displacement measurement of beam-like supertall structures using acceleration and strain sensors. Struct Health Monit 2020;19(2):520–36. https://doi.org/10.1177/1475921719857043.

[67] Zhou Q, Li Q, Han X-L, Wan J-W, Xu K. Horizontal displacement estimation of high-rise structures by fusing strain and acceleration measurements. Build Eng 2022;57:104964. https://doi.org/10.1016/j.jobe.2022.104964.

[68] Ma Z, Choi J, Sohn H. Continuous bridge displacement estimation using millimeter-wave radar, strain gauge and accelerometer. Mech Syst Signal Pr 2023; 197:110408. https://doi.org/10.1016/j.ymssp.2023.110408.

[69] Li D, Sang Y, Lv Z, Wu K, Lai Z. Dynamic response analysis of wind turbine tower with high aspect ratio: Wind tunnel tests and CFD simulation. Thin-Walled Struct 2025;211:113113. https://doi.org/10.1016/j.tws.2025.113113.

[70] Pagnini LC. A numerical approach for the evaluation of wind-induced effects on inclined, slender structural elements. Eur J Environ Civ Eng 2017;21(7-8):854–73. https://doi.org/10.1080/19648189.2016.1164088.

[71] Solari G, Repetto MP. General tendencies and classification of vertical structures under gust buffeting. J Wind Eng Ind Aerodyn 2002;90:1299–319. https://doi.org/10.1016/S0167-6105(02)00259-3.

[72] Holmes JD. Wind loading of structures. CRC Press, Taylor & Francis Group, NY. 2015. https://doi.org/10.1201/b18029.

[73] Vickery BJ. On the reliability of gust loading factors. Proc., Technical Meeting Concerning Wind Loads on Buildings and Structures. Washington, DC: National Bureau of Standards; 1970. p. 93–104.

[74] Simiu E. Revised procedure for estimating along-wind response. ASCE J Struct Div 1980;106(1):1–10. https://doi.org/10.1061/jsdeag.0005329.

[75] Solari G. Alongwind response estimation: closed form solution. ASCE J Struct Div 1982;108:225–44. https://doi.org/10.1061/JSDEAG.0005861.

[76] Tamura Y, Kawai H, Taniike Y. Wind load and wind-induced response estimations in the Recommendations for loads on buildings, AIJ 1993. Eng Struct 1996;18: 339–411. https://doi.org/10.1016/0141-0296(95)00121-2.

[77] Solari G. Gust buffeting. I: Peak wind velocity and equivalent pressure. J Struct Eng-ASCE 1993;119(2):365–82. https://doi.org/10.1061/(ASCE)0733-9445(1993)119:2(365).

[78] Zou L, Qiu F, Xu G, Shi T, Kareem A. Contribution of the second mode to wind-induced response of prismatic tall buildings. Eng Struct 2025;322:119202. https://doi.org/10.1016/j.engstruct.2024.119202.

[79] Pagnini L. Reliability analysis of wind-excited structures. J Wind Eng Ind Aerodyn 2010;98(1):1–9. https://doi.org/10.1016/j.jweia.2009.08.010.

[80] Solari G. Wind-excited response of structures with uncertain parameters. Probab Eng Mech 1997;12(2):75–87. https://doi.org/10.1016/S0266-8920(96)00027-6.

[81] Pagnini LC, Repetto MP. The role of parameter uncertainties in the damage prediction of the alongwind-induced fatigue. J Wind Eng Ind Aerodyn 104106 2012:227–38. https://doi.org/10.1016/j.jweia.2012.03.027.

[82] ESDU 84011 2012. Wind speed profiles over terrain with roughness changes. London, UK.

[83] Flay RGJ, Stevenson DC. Integral length scales in strong wind below 20m. Advances in Wind Engineering 1988;28(1-3):21–30. https://doi.org/10.1016/0167-6105(88)90098-0.

[84] Orlando A, Pagnini L, Repetto MP. Wind tunnel tests of a hexadecagonal cylinder with imperfections and ancillaries: aerodynamic characterization and technical discussion. Eng Struct 2023;274:115114. https://doi.org/10.1016/j.engstruct.2022.115114.

[85] ESDU 79026. Mean fluid forces and moments on cylindrical structures. London, UK: polygonal sections with rounded corners including elliptical shape; 1980.

[86] Li D, Fang S, Sun C, Xu F, Zhao J, Lai Z. Aeroelastic wind tunnel study and numerical simulation of concrete-filled double-skin tubular (CFDST) wind turbine system. Structures 2025;74:108581. https://doi.org/10.1016/j.istruc.2025.108581.

[87] Pagnini L, Piccardo G. Modal properties of a vertical axis wind turbine in operating and parked conditions. Eng Struct 2021;242:112587. https://doi.org/10.1016/j.engstruct.2021.112587.

[88] Orlando A, Pagnini L, Repetto MP. Structural response and fatigue assessment of a small vertical axis wind turbine under stationary and non-stationary excitation. Renew Energ 2021;170:251–66. https://doi.org/10.1016/j.renene.2021.01.123.

[89] Pagnini L, Orlando A, Repetto MP. Damping assessment of monopole steel structures through full-scale experiments. Eng Struct 2025;327:119627. https://doi.org/10.1016/j.engstruct.2025.119627.

[90] Brincker R, Ventura C. Introduction to Operational Modal Analysis. UK: John Wiley & Sons; 2015.

[91] Brincker R, Zhang L, Andersen P. Modal identification of output-only systems using frequency domain decomposition. Smart Mater Struct 2001;10:441–5. https://doi.org/10.1088/0964-1726/10/3/303.

[92] Kwon DK, Kareem A, Stansel R, Ellingwood BR. Wind load factors for dynamically sensitive structures with uncertainties. Eng Struct 2015;103:53–62. https://doi.org/10.1016/j.engstruct.2015.08.031.

[93] Pagnini L. Model reliability and propagation of frequency and damping uncertainties in the dynamic alongwind response of structures. –31 J Wind Eng Ind Aerodyn 1996;59(2,3):211. https://doi.org/10.1016/0167-6105(96)00008-6.

[94] Pagnini L, Piccardo G, Solari G. VIV regimes and simplified solutions by the spectral model description. J Wind Eng Ind Aerodyn 2020 2020;198:104100. https://doi.org/10.1016/j.jweia.2020.104100.

[95] Brusco S, Bagnara A, Cammelli S, Piccardo G. Experimental investigations on the vortex-shedding from a highly tapered circular cylinder in smooth flow. J Fluids Struct 2023;122:103983. https://doi.org/10.1016/j.jfluidstructs.2023.103983.